The metallophilic interaction between cyclometalated complexes: photobiological applications

Zhou, X.

3

The self-assembly of a cyclometalated palladium photosensitizer into proteins-stabilized nanorods triggered drug uptake in vitro and in vivo

Enhanced passive diffusion is usually considered as the primary cause for the enhanced cellular uptake of cyclometalated drugs, because cyclometalation lowers the charge of a metal complex and increases its lipophilicity. However, in this work, the monocationic cyclometalated palladium complexes ***[1]OAc*** *(**N^N^C^N**) and* ***[2]OAc*** *(**N^N^N^C**) were found to self-assemble, in aqueous solutions, into soluble supramolecular nanorods, while their tetrapyridyl dicationic analogue* ***[3](OAc)₂*** *(**N^N^N^N**) dissolved as isolated molecules. These nanorods formed via metallophilic Pd…Pd interaction and π-π stacking, and were stabilized in cell medium by serum proteins, in absence of which the nanorods precipitated. In cell cultures these protein-stabilized self-assembled nanorods were responsible for the improved cellular uptake of the cyclometalated compounds, which took place via endocytosis, i.e. an active uptake pathway. In addition to triggering self-assembly, cyclometalation in* ***[1]OAc*** *also led to dramatically enhanced photodynamic properties under blue light irradiation. These combined penetrations and photodynamic properties were observed in multicellular tumor spheroids and a mice tumor xenograft, demonstrating that protein-stabilized nanoaggregation of cyclometalated drugs such as* ***[1]OAc*** *allows efficient cellular uptake also in 3D tumor models. Overall, serum proteins appear as a major element of drug design, as they strongly influence the size and bioavailability of supramolecular drug aggregates, and hence their efficacy in vitro and in vivo.*

This chapter has been accepted for publication as a full paper and front cover: X.-Q. Zhou, M. Xiao, V. Ramu, J. Hilgendorf, X. Li, P. Papadopoulou, M. A. Siegler, A. Kros, W. Sun* and S. Bonnet*, ***J. Am. Chem. Soc.***, 2020, **142**, 23, 10383-10399.

3.1 Introduction

Research on metal-based anticancer drugs has been encouraged for many years by the clinical success of cisplatin, carboplatin, oxaliplatin, and nedaplatin, four metal-based drugs used in the treatment of cancer.[1-3] However, the similar mode of action of these platinum-based compounds, where aquation of some of the leaving groups by intracellular water leads to nonselective covalent binding of platinum to DNA, results in significant side effects and drug resistance.[3-10] Several strategies have been developed to overcome these drawbacks, in particular photodynamic therapy (PDT). PDT is a fast-developing cancer treatment modality because it shows reduced systemic cytotoxicity to cancer patients.[11-13] In PDT, a photosensitizing agent (PS) is injected, and upon light at the tumor site, cytotoxic reactive oxygen species (ROS) are generated via a so-called type I (electron transfer) mechanism, or via a type II (energy transfer) pathway.[14-19] These two competing pathways may also occur simultaneously, and the ratio between these processes depends on many parameters such as the type of PS used, the concentrations of substrate, and dioxygen (O_2), the localization of the photosensitizer.[14, 16] In the design of new PSs, metal complexes derived from heterocyclic ligands, especially polypyridyl ligands, have attracted a great amount of attention due to their tunable photophysical properties and their visible light absorption, which greatly improve the light penetration of biological tissues compared to that of UV-light-sensitive molecules.[13, 20-24] Short-wavelength (blue or green) PDT agents, although traditionally considered to be academic curiosities due to the low tissue penetration of this type of visible light, are regaining interest for certain cancers of thin organs, such as skin and bladder, because the thickness of the tumors in such cancers matches the penetration depth of blue light and green light well.[25]

More particularly, cyclometalated metal complexes, in which a metal-nitrogen bond is replaced by a metal-phenylene bond, have been considered to be a way to improve the efficiency of metal-based PDT sensitizers. Cyclometalated complexes are indeed known for the significant red-shift of their absorption maxima compared to that of polypyridyl analogues, enhanced stability in solution, and improved cellular uptake.[26] The latter is usually claimed to be due to their decreased charge and increased lipophilicity compared to those of polypyridyl analogues .[20, 26] However, little is known for the fate of cyclometalated metal complexes in cell medium, which is a complex mixture of many small biological molecules and proteins.[27] These biomolecules might interact with cyclometalated complexes to generate either new molecular species or supramolecular aggregates, resulting in modified cellular uptake and biological properties.[28, 29] Recently, Thomas's group reported a series of cyclometalated $[Ir^{III}Ru^{II}]^{3+}$

luminescent DNA imaging probes that were prevented to penetrate the nuclei of cancer cells by reaction with the serum albumin present in cell growing medium, while their polypyridyl analogue $[Ir^{III}Ru^{II}]^{4+}$ retained nuclear staining properties in serum-containing medium.[30] Che's group also reported a self-assembled platinum/gold system for controlled drug release and accumulation in tumors.[31] Coincidentally, many cyclometalated complexes in the literature have been shown to produce fluorescent dots in the cytoplasm and not to reach the nucleus,[31-33] an organelle that selectively sorts out particles of small sizes.[34]

Palladium(II) complexes have been proposed as possible analogues of antitumor platinum complexes for their similar d^8 coordination sphere and tetradentate square-planar structure. Recently, two palladium-based PDT sensitizers, Padoporfin and its derivative Padeliporfin, have been clinically approved to treat prostate cancer, which demonstrates the potential of palladium complexes for PDT.[15, 35] Encouraged by these developments, our group recently studied the influence of the position of the Pd-C bond in cyclometalated palladium complexes based on tetrapyridyl ligand Hbbpya (N,N-bis(2,2′-bipyrid-6-yl)amine), with respect to their photodynamic properties.[36] The isomer characterized by a Pd-C bond on the side of the noncoordinated NH bridge of this ligand shows better blue-light absorption and a better singlet oxygen generation ability, compared to the isomer where the Pd-C bond lies further from the NH bridge. However, in these complexes the deprotonation of the noncoordinated NH bridge becomes easy upon palladation of the ligand, resulting in insoluble neutral metal complexes, thus limiting their application for cancer treatment *in vivo*. In this work, we methylated this NH bridge and synthesized three analogous palladium complexes: cyclometalated isomers **[1]OAc** (N^N^C^N coordination) and **[2]OAc** (N^N^N^C coordination), and the reference tetrapyridyl complex **[3](OAc)$_2$** (N^N^N^N coordination, Scheme 3.1). All palladium complexes, prepared with acetate counterion, were water-soluble. With this new series of complexes at hand, it was possible to address the influences of cyclometalation and isomerism on the aggregation and fate of these metal complexes *in vitro* and *in vivo* and to study how proteins present in serum influenced their speciation and uptake.

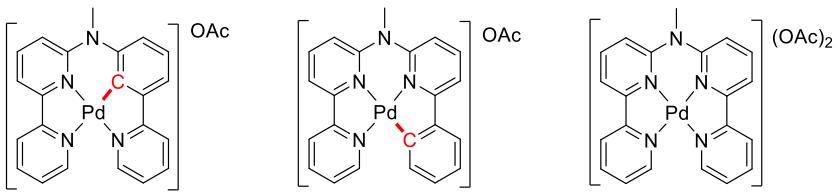

Scheme 3.1 *Structures of the metal complexes.*

3.2 Results

3.2.1. Synthesis and characterization. The three titled palladium complexes **[1]**$^{+}$**-[3]**$^{2+}$ were synthesized as acetate salts by reacting methylated ligands **MeL**^{1}, **MeL**^{2}, and **MeL**^{3} with palladium acetate (Scheme AII.1). All complexes were obtained in high yield without chromatography and were characterized by NMR, HRMS, elemental analysis, and single-crystal X-ray diffraction (APPENDIX II). The acetate counteranion provided good water solubility and similar log P_{ow} values of -1.88, -1.92, and -1.71, respectively. These values suggested similar cellular uptake efficacy if the three molecules would remain as monomers in aqueous solutions. It is noteworthy that the ^{1}H NMR spectra of cyclometalated complexes **[1]**$^{+}$ and **[2]**$^{+}$ showed significant differences at low and high concentrations, while **[3]**$^{2+}$ did not show this effect (Figure AII.1). Thus, NMR suggested that cyclometalation may promote aggregation in this type of complex.[37, 38]

Single crystals of **[1]PF$_6$**, **[2]PF$_6$**, and **[3](BF$_4$)$_2$**, were obtained by the slow evaporation of a MeCN/EtOAc solution or by vapor diffusion from diethyl ether to a MeCN/EtOAc solution. The crystals were analyzed by single-crystal X-ray diffraction. Crystallographic data and a selection of interatomic distances and angles are shown in Table AII.1 and Table 3.1, respectively. All three complexes crystallized in the triclinic *P-1* space group. As shown in Figure 3.1a, **[1]PF$_6$** and **[2]PF$_6$** were coordination isomers, with three nitrogen atoms and one carbon atom coordinated to the palladium(II) cation and bond lengths in the range 1.9786(18)-2.1086(17) Å. Four nitrogen atoms are coordinated to palladium in reference complex **[3](BF$_4$)$_2$.** The coordination sphere of these three complexes was slightly distorted, as shown by the small dihedral angle in complexes **[1]PF$_6$** (N1-N2-C17-N4 = 3.96°), **[2]PF$_6$** (N1-N2-N4-C22=2.91°), and **[3](BF$_4$)$_2$** (N1-N2-N4-N5=5.42°). τ_4, a structural parameter used to distinguish square-planar from tetrahedral coordination complexes (τ_4=360°-(α+β)/(141°), where α and β are the two greatest valence angles of the coordination sphere),[39] was 0.112 for **[1]PF$_6$**, 0.109 for **[2]PF$_6$**, and 0.097 for **[3](BF$_4$)$_2$**, suggesting that these complexes are essentially square planar. The two cyclometalated, monocationic palladium complexes, also showed clear π-π* stacking and short Pd-Pd distances (3.275 Å-4.316 Å), suggesting the occurrence of Pd…Pd metallophilic interaction.[40] In contrast, the reference complex **[3](BF$_4$)$_2$** had higher Pd…Pd distances (6.814 Å-8.373 Å) that were almost twice as long, indicating the absence of Pd…Pd interaction in this dicationic compound (Figure 3.1b). Interestingly, these metal-metal interactions stimulate the cyclometalated complexes **[1]PF$_6$**, **[2]PF$_6$** to self-assemble.[41-43]

Overall, X-ray crystallography was consistent with NMR results and suggested that Pd…Pd metallophilic interaction may occur both in solution and in the solid state.

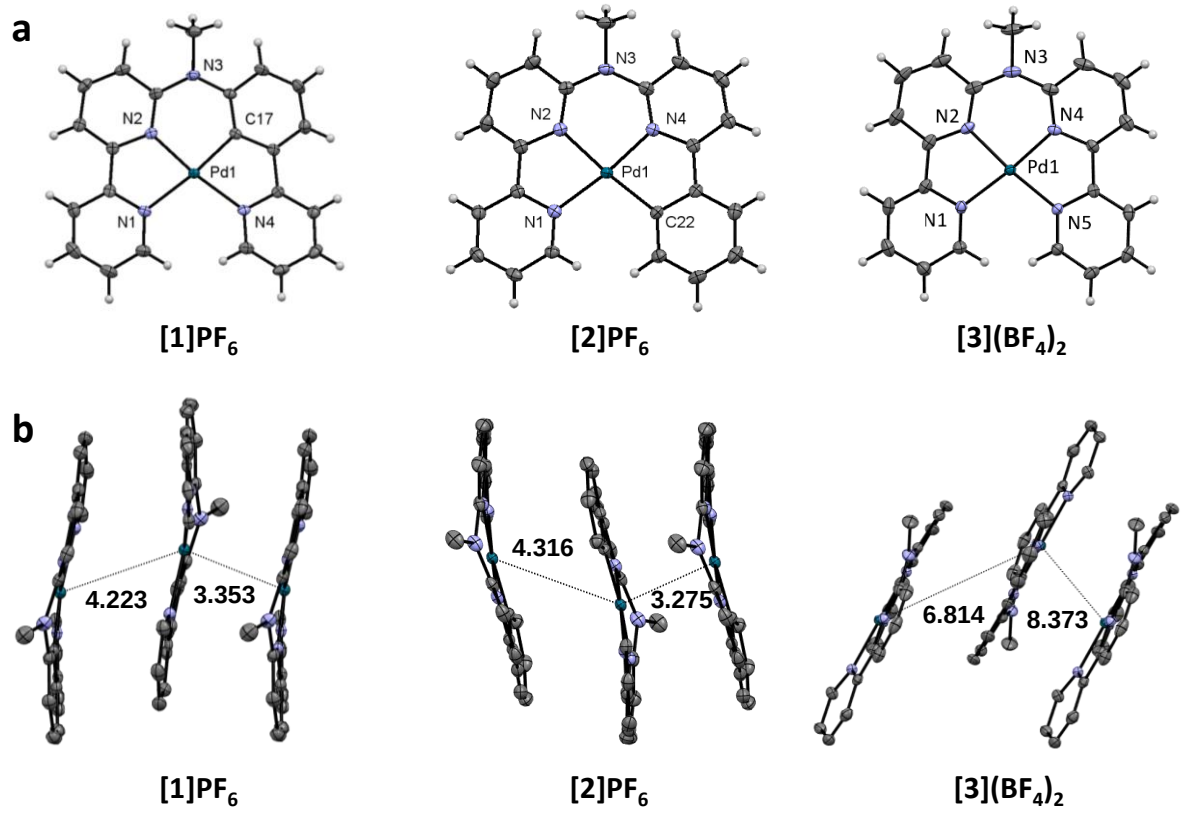

Figure 3.1 *Molecular view of the cationic complexes (a) and their stacking (b) in the crystal structures of* ***[1]PF$_6$****,* ***[2]PF$_6$****, and* ***[3](BF$_4$)$_2$****. Displacement ellipsoids are shown at the 50% probability level. Pd…Pd distances are indicated in angstroms. Counterions and disorder have been omitted for clarity.*

Table 3.1 *Selected bond distance (angstroms) and angles (degrees) of* ***[1]PF$_6$****,* ***[2]PF$_6$*** *and* ***[3](BF$_4$)$_2$****.*

[1]PF$_6$		**[2]PF$_6$**		**[3](BF$_4$)$_2$**	
Pd-N1	2.1086(17)	Pd-N1	2.0544(18)	Pd-N1	2.048(2)
Pd-N2	1.9860(19)	Pd-N2	2.0435(18)	Pd-N2	1.979(2)
Pd-C17	1.9786(18)	Pd-N4	2.0096(18)	Pd-N4	1.983(2)
Pd-N4	2.0912(18)	Pd-C22	2.019(2)	Pd-N5	2.034(2)
Pd-Pd	4.223, 3.353	Pd-Pd	4.316, 3.275	Pd-Pd	6.814, 8.373
N1-Pd-N2	81.00(7)	N1-Pd-N2	80.88(7)	N1-Pd-N2	81.75(9)
N2-Pd-C17	92.19(8)	N2-Pd-N4	92.04(7)	N2-Pd-N4	92.97(9)
C17-Pd-N4	80.94(7)	N4-Pd-C22	82.33(8)	N4-Pd-N5	81.67(9)
N4-Pd-N1	105.77(7)	C22-Pd-N1	104.52(8)	N5-Pd-N1	103.64(9)

3.2.2. Photophysical characterization and frontier orbitals. The photophysical properties of **[1]OAc-[3](OAc)$_2$** in water are shown in Figure 3.2 and Table 3.2. Importantly (see below), under such conditions none of the molecules aggregate. Both complexes **[2]$^+$** and **[3]$^{2+}$** showed intense absorbance essentially in the ultraviolet range (300-400 nm), but a bathochromically-shifted absorption band was observed for **[1]$^+$**, characterized by an absorption maximum at 428 nm. As a result, in pure water the molar absorptivity values at 455 nm for the three complexes were 1500, 37 and 56 M^{-1} cm^{-1}, respectively, indicating that while **[2]$^+$** or **[3]$^{2+}$** are bad blue light PDT sensitizers, **[1]$^+$** may be good at it. The difference in blue light absorption can be explained by the different HOMO-LUMO orbital energy gaps of the three compounds. According to DFT at the PBE0/TZP/COSMO level (Figure AII.2, Table AII.2) the HOMO and LUMO orbitals of all three complexes have π symmetry and have a very low (5.55% for **[1]$^+$**) to zero (for **[2]$^+$** and **[3]$^{2+}$**) contribution of the palladium centers. The HOMO is centered on the noncoordinated amine bridge NMe of the ligand, and in the two cyclometalated complexes, its energy is strongly affected by how close the electron-rich Pd-C$^-$ bond is to NMe (E_{HOMO} = -6.24 eV for **[1]$^+$**, -6.58 eV for **[2]$^+$**). On the other hand, the LUMO is based on the bipyridine fragment of the ligand and its energy is hence essentially independent of the position of the electron-rich Pd-C$^-$ bond (E_{LUMO} = -2.41eV for **[1]$^+$**, -2.46 eV for **[2]$^+$**). For **[3]$^{2+}$**, the HOMO was slightly stabilized compared to that of **[2]$^+$** due to the more electron-poor nature of the tetrapyridyl ligand, compared to its cyclometalated version (Table AII.2). The resulting HOMO-LUMO energy gaps of the three complexes follow the series **[1]$^+$ (3.83 eV) << [2]$^+$ (4.11 eV) < [3]$^{2+}$ (4.13 eV)**, which explains the better absorption of **[1]$^+$** in the blue region of the spectrum. These results were confirmed by time-dependent density functional theory calculations (TDDFT, see Figure AII.3). Compounds **[1]$^+$-[3]$^{2+}$** showed their lowest-energy transitions at 412, 368 and 369 nm, respectively, and these lowest-energy transitions corresponded to 97.5%, 95.2% and 98.1%, respectively, for the HOMO→LUMO transition. The excited states of these complexes, which must be of triplet multiplicity considering the heavy nature of the palladium atom and the efficient formation of $^1O_2$ (see below), hence have intraligand charge transfer character (^{3}ILCT). The phosphorescence emission from these states was similarly weak and very short in aerated Milli-Q solutions (Figure 3.2a), with quantum yields (φ_P) lower than 0.5% and lifetimes between 150 and 310 ps (Table 3.2, Figure AII.4). However, their quantum yields for $^1O_2$ generation (φ_Δ), which were measured under 450 nm excitation by direct detection of the 1274 nm infrared emission of $^1O_2$ in CD_3OD, were very different (Figure 3.2b, Table 3.2). **[1]$^+$** showed the best $^1O_2$ quantum yield (0.78, compared to 0.73 for the reference **[Ru(bpy)$_3$]Cl$_2$**),[44] followed by **[2]$^+$** (0.052) and finally **[3]$^{2+}$** (0.009).

Overall, **[1]**$^{+}$ shows excellent properties for blue-light PDT, including good light absorption around 450 nm and excellent $^{1}O_2$ generation efficiency in air, while **[2]**$^{+}$ is only slightly better than **[3]**$^{2+}$, which has negligible photodynamic properties.

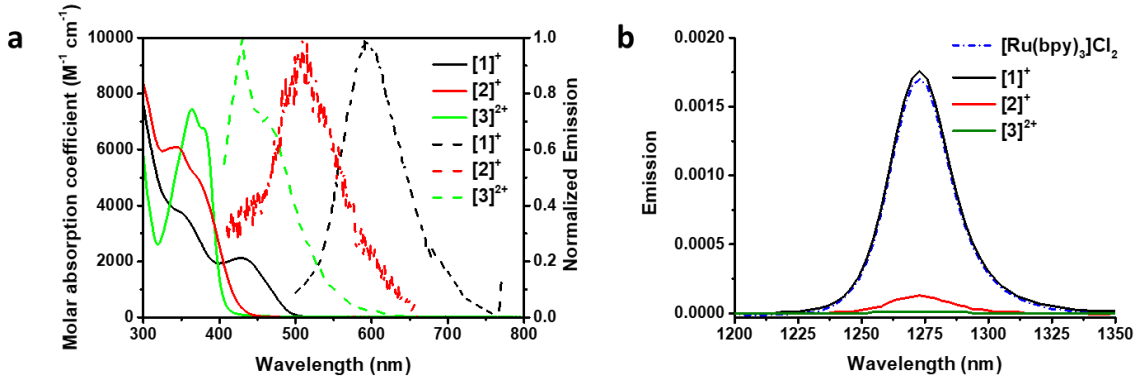

Figure 3.2 *(a) Absorption (solid line, left axis) and normalized emission spectra (dashed line, right axis) of* ***[1]OAc-[3](OAc)$_2$*** *in water (50 µM, 350 nm excitation). (b) Singlet oxygen emission for solutions of* ***[1]$^{+}$-[3]$^{2+}$*** *in CD_3OD (450 nm excitation, A_{450} = 0.1).*

Table 3.2 *Photophysical data for complexes* ***[1]OAc-[3](OAc)$_2$****.*

Complex	λ_{abs}, nm ($\varepsilon \times 10^3$ M^{-1} cm^{-1})[a]	λ_{em} (nm)[a]	φ_P	Lifetime (ns)[a,d] τ_1	τ_2	φ_Δ[e]
[1]OAc	428 (2.12), 455 (1.50)	593	0.0029 [b]	0.159 ± 0.003	–	0.78 [f] 0.73 [g]
[2]OAc	344 (6.10), 455 (0.037)	509	0.00038 [b]	0.211 ± 0.008	–	0.052 [f]
[3](OAc)$_2$	364 (7.45), 455 (0.056)	430	0.0038 [c]	0.309 ± 0.003 (87%)	4.17 ± 0.08 (13%)	0.009 [f]

[a] Measurements were carried out in Milli-Q water. [b] Phosphorescence quantum yield measurements of **[1]**$^{+}$**-[2]**$^{+}$ were carried out at a 390 nm excitation wavelength in aerated water, using [Ru(bpy)$_3$]Cl$_2$ (φ_P = 0.028) as the standard.[45] [c] Phosphorescence quantum yield measurement of **[3]**$^{2+}$ was carried out at 350 nm excitation wavelength in aerated ethanol, using 9,10-diphenylanthracene (φ_P = 0.885) as the standard.[45] [d] Excitation wavelength 375 nm. [e] Excitation wavelength 450 nm, air atmosphere. The absorption of each complex at 450 nm was adjusted to 0.1 to avoid the generation of excimer. [f] In CD_3OD by spectroscopic detection at 1270 nm; [Ru(bpy)$_3$]Cl$_2$ was used as the standard (φ_Δ = 0.73).[46] [g] In Opti-MEM complete using 9,10-anthracenediyl-bis(methylene)dimalonic acid as the $^{1}O_2$ probe; **[Ru(bpy)$_3$]Cl$_2$** was used as standard (φ_Δ = 0.14; see Figure AII.2).

3.2.3 Aggregation of the metal complexes in cell culture medium. In this family of palladium complexes, cyclometalation of dicationic complex **[3]**$^{2+}$ lowers its charge from +2 to +1, which

influences the supramolecular interaction of the metal complexes with itself and with other charged biomolecules. The NMR and crystallographic studies discussed above stimulated us to compare the behavior of complexes **[1]**$^{+}$**-[3]**$^{2+}$ at 5 or 50 µM in a series of biomimetic solvents: H_2O, PBS, Opti-MEM cell medium with 2.5% fetal calf serum (FCS; this mixture is hereafter Opti-MEM complete), and Opti-MEM without FCS. The formation of nanoaggregation in the biomimetic solvents was studied with dynamic light scattering (DLS). All three palladium complexes dissolved well in water and PBS solution, as shown by the low DLS derived count rate (in kcps), indicating that no aggregation occurred under these conditions (Figure 3.3a, Table AII.5). In contrast, in the presence of Opti-MEM cell medium with or without FCS, cyclopalladated complexes **[1]**$^{+}$**-[2]**$^{+}$ aggregating into particles, with a 35-fold (5 µM) or 102-fold (50 µM) increase in the derived countrate values. However, the derived count rate for **[3]**$^{2+}$ in all biomimetic solvents remained at a low level. The different behavior of complexes **[1]**$^{+}$**-[3]**$^{2+}$ in Opti-MEM demonstrates the significant influence of cyclometalation and complex charge on the aggregation properties of these palladium complexes. Besides, the size of the aggregates made in the **[1]**$^{+}$**-[2]**$^{+}$ in medium utterly depended on the presence of serum proteins (Figure 3.3b, AII.5). In the medium with FCS, the particle distribution maximum was 458 nm and 396 nm at 50 µM concentration (Figure 3.3b). In the absence of FCS, microparticles (hydrodynamic diameter > 1000 nm) were formed, resulting in precipitation (Figure 3.3c). Upon increasing the palladium complex concentration from 5 to 50 µM, the nanoparticles around 10-100 nm, which belong to the FCS proteins, almost disappeared and were replaced by micrometer-sized particles (Figure AII.5). For the dicationic complex **[3]**$^{2+}$ no significant changes occurred in the DLS analysis when the concentration was varied from 5 µM to 50 µM in all solutions, showing the absence of aggregation for this dicationic compound (Figure 3.3, AII.5). Meanwhile, the acidic nature of cancer cells[47] stimulated us to observe the aggregation behavior of **[1]OAc** in cell medium at different pH values (3.30-7.64). As shown in Figure AII.6, **[1]**$^{+}$ still formed nanoaggregates (100-1000 nm) while the size distribution maximum slightly increased with pH, suggesting possible aggregation of this compound in the more acidic environment of cancer cells or lysosome.

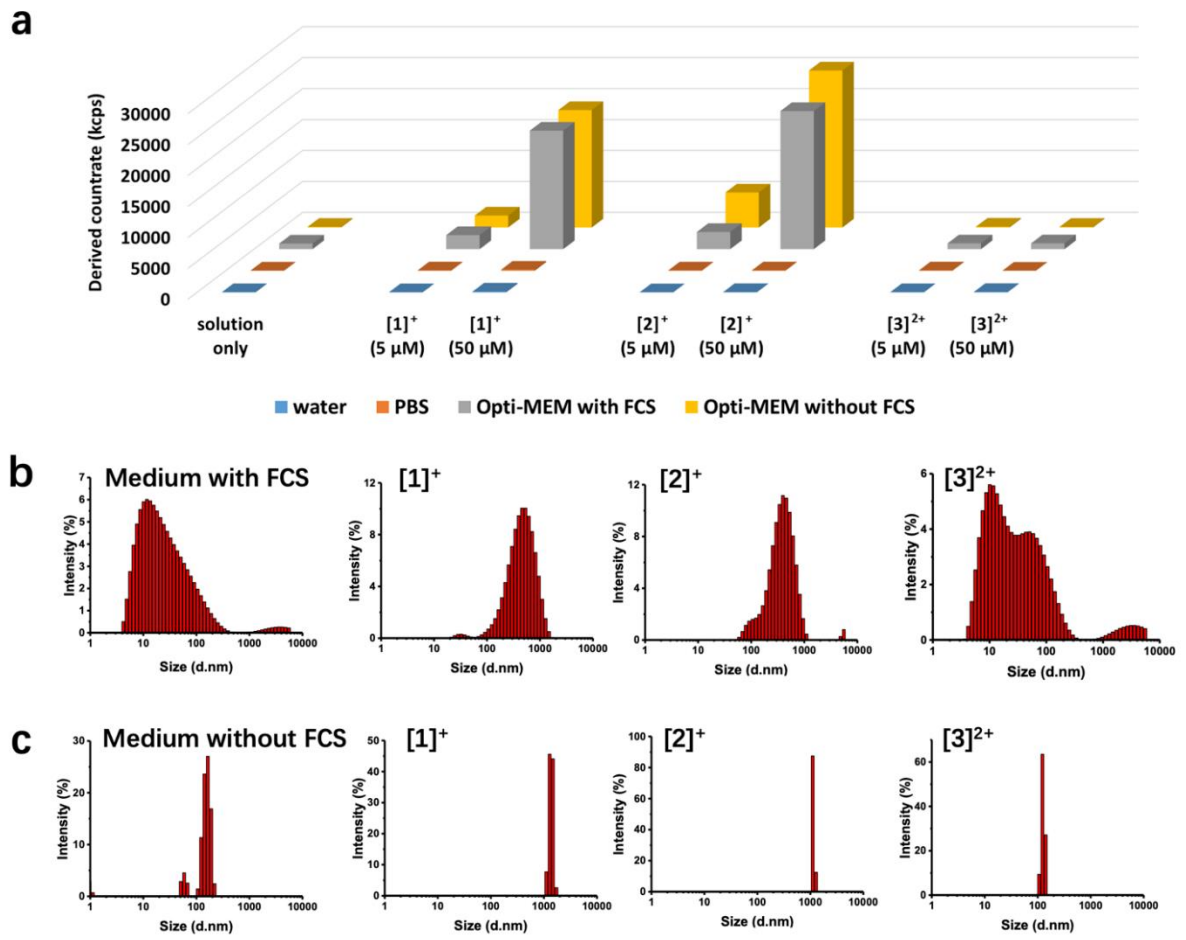

Figure 3.3 *(a) Dynamic light scattering derived count rate of* ***[1]*****$^{+}$****-****[3]*****$^{2+}$** *at 5 or 50 µM in pure water, PBS, and Opti-MEM medium with or without FCS (2.5% v/v); Size distribution of the DLS analysis of solutions of* ***[1]*****$^{+}$****-****[3]*****$^{2+}$** *(50 µM) in Opti-MEM medium with (b) or without (c) FCS. The X-axis is the hydrodynamic diameter (in nm); the Y-axis is intensity (%).*

Another view of the chemical stability and aggregation behavior of these complexes in the different media was provided by following in time the absorbance spectra of solutions of **[1]**$^{+}$**-[3]**$^{2+}$ in H_2O, PBS, and Opti-MEM cell medium with or without FCS (Figure AII.7). All complexes were stable in water and PBS solutions for 24 h, confirming that the tetradentate nature of the ligand prevents the coordination of water or chloride ligands to the metal center. In addition, the complexes were stable in the presence of GSH and ascorbic acid (Figure AII.7), showing that palladium(II) was not reduced under such conditions. In cell medium with FCS, **[1]**$^{+}$**-[2]**$^{+}$ showed significant increases in the baseline absorbance over 24 h, which can be attributed to increased scattering by the nanoparticles forming in solutions.[48] In contrast, in the medium without FCS the absorbance decreased quickly during the first 15 min and remained essentially constant in a second step, which can be assigned to precipitation. For **[3]**$^{2+}$, the

absorbance did not vary significantly in the medium without FCS, confirming the higher solubility of the dicationic complex. However, in FCS-containing medium a dramatic change was observed, characterized by an isosbestic point at 358 nm, indicating a chemical reaction between **[3]$^{2+}$** and one of the components of FCS. These results matched the observations made by DLS (*i.e.* **[1]$^{+}$-[2]$^{+}$** precipitated in medium without FCS but generated ~400 nm hydrodynamic diameter nanoparticles when FCS was added to the cell medium). This result suggests that the proteins present in FCS play a dramatic role in the aggregation state of cyclopalladated compounds **[1]$^{+}$-[2]$^{+}$,** while for tetrapyridyl complex **[3]$^{2+}$** this role is much less pronounced. We can hence expect a different mechanism of cell uptake for monocationic complexes **[1]$^{+}$-[2]$^{+}$** compared with dicationic compound **[3]$^{2+}$** because many cell uptake pathways, including endocytosis, depend on the size of drugs.[49, 50] Besides, the aggregation of **[1]$^{+}$-[2]$^{+}$** in an FCS-containing medium suggests that upon injection into the bloodstream of a mammal these types of cyclometalated compounds may generate protein-caped nanoparticles, which may influence the tumor uptake and biological half-time of cyclometalated compounds compared to nonaggregated small molecules such as **[3]$^{2+}$**.

3.2.4 Supramolecular polymerization of cyclometalated complexes. If the data above demonstrated that nanoaggregates were stabilized in FCS-containing medium, it was not clear yet as to whether the palladium complex or proteins abundant in serum, such as albumin, were responsible for aggregate formation. As **[1]OAc-[3](OAc)$_2$** do not form aggregates in pure water, and form them too quickly in Opti-MEM complete, we changed their counteranion to hexafluorophosphate by reprecipitation with KPF_6 to make them less hydrophilic, which allowed for observing the kinetics of the formation of the nanorods. Supramolecular live polymerization of **[1]PF$_6$**, and **[2]PF$_6$** was observed in H_2O/MeCN solution (100 µM, 9:1, v/v) via UV-vis absorption spectroscopy.[42] As shown in Figure 3.4a, b, d, for **[1]PF$_6$** and **[2]PF$_6$** the baseline of the absorbance spectrum increased quickly (within 6 to 7 min), suggesting increasing light scattering; it then stabilized until the end of the experiment (t=30 min). By contrast, the absorbance of **[3](PF$_6$)$_2$** showed only negligible variations (Figure 3.4c, d). At the end of these UV-vis experiments, each solution was deposited on a TEM grid to observe the morphology of the nanoaggregates by TEM. Complexes **[1]PF$_6$** and [**2]PF$_6$** showed beautiful nanorod morphologies, while **[3](PF$_6$)$_2$** showed random aggregates reminiscent of a precipitate. These data clearly show that the cyclometalated complexes **[1]$^{+}$-[2]$^{+}$** themselves can self-assemble into nanorods most probably due to the Pd…Pd interaction observed in the solid state.

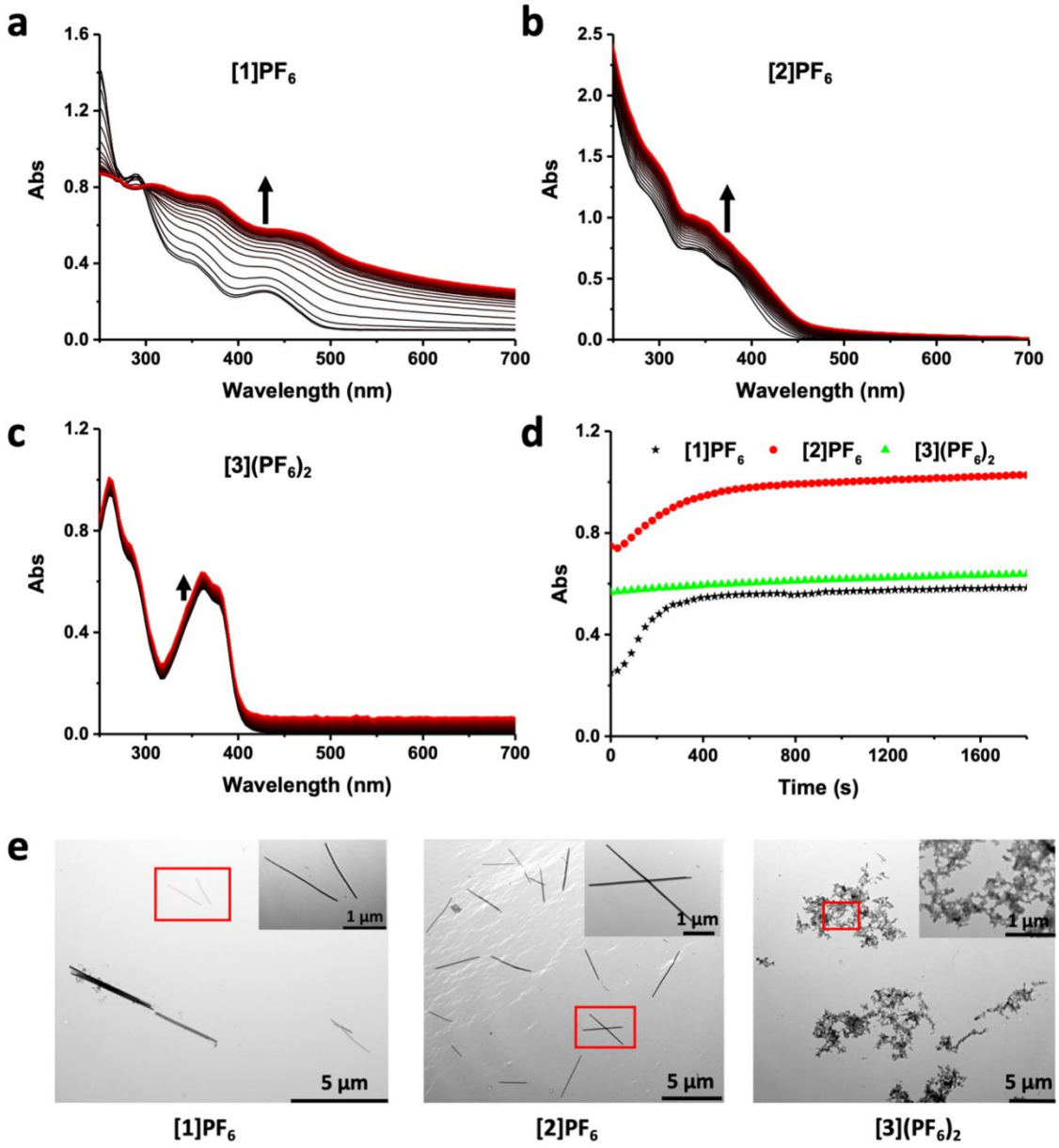

Figure 3.4 *Time evolution of the absorption spectra of the H_2O/MeCN solution (100 µM, 9:1, v/v) of complexes* ***[1]PF$_6$*** *(a),* ***[2]PF$_6$*** *(b), and* ***[3](PF$_6$)$_2$*** *(c) at 298 K for 30 min; (d) Time evolution of the absorption at 428 nm (black stars,* ***[1]PF$_6$****), 332 nm (red dots,* ***[2]PF$_6$****), 360 nm (green triangles,* ***[3](PF$_6$)$_2$****) of these solutions. The absorption spectra were measured every 30 s. (e) TEM images of* ***[1]PF$_6$*** *(a),* ***[2]PF$_6$*** *(b), and* ***[3](PF$_6$)$_2$*** *after aggregation in the H_2O/MeCN solution (100 µM, 9:1, v/v) for 30 min (scale bar 5 µm, inset 1 µm).*

3.2.5 Cryo-TEM measurements in Opti-MEM medium. Compounds **[1]OAc-[3](OAc)$_2$** dissolve well in water with a low derived count rate according to DLS (Figure 3.3a). TEM gives a higher-contrast picture: while samples of **[1]OAc-[2]OAc** prepared from a Milli-Q water solution (50 µM) showed rectangular nanorods with an average length of around 139 and 203

nm, respectively, samples of **[3](OAc)$_2$** at the same concentration showed random shapes characteristic of a precipitate (Figure AII.8). In both cases, the observed particulates were artifacts due to the evaporation of solvent before TEM imaging. Cryo-TEM, on the contrary, allows for observing nanostructures directly as they are in solution (*i.e.* in their native state). Cryo-TEM images of a 50 µM solution of **[1]OAc-[3](OAc)$_2$** under different conditions were hence recorded. As shown in Figure 3.5 and Figure AII.9, the two cyclometalated compounds **[1]OAc-[2]OAc** in Opti-MEM did generate nanorods characterized by a width of ~20 nm. In the presence of FCS, these nanorods were nicely dispersed on the grid or were forming aggregates of about 500 nm, while in the absence of FCS they aggregated in much larger aggregates of micrometer size. Compound **[3](OAc)$_2$**, on the contrary, did not show such nanorods. Interestingly, when **[1]OAc** (50 µM) was dispersed in pure FCS solution, bent nanofibers were observed, indicating that the proteins contained in FCS also played a role in the generation of nanostructures. Overall, all cryo-TEM images were fully consistent with the DLS results. From these data, it appears that FCS stabilized nanorods in the cell medium for cyclometalated compounds **[1]OAc-[2]OAc** while in the absence of FCS the nanorods aggregate with each other into larger clusters that end up precipitating out of solution.

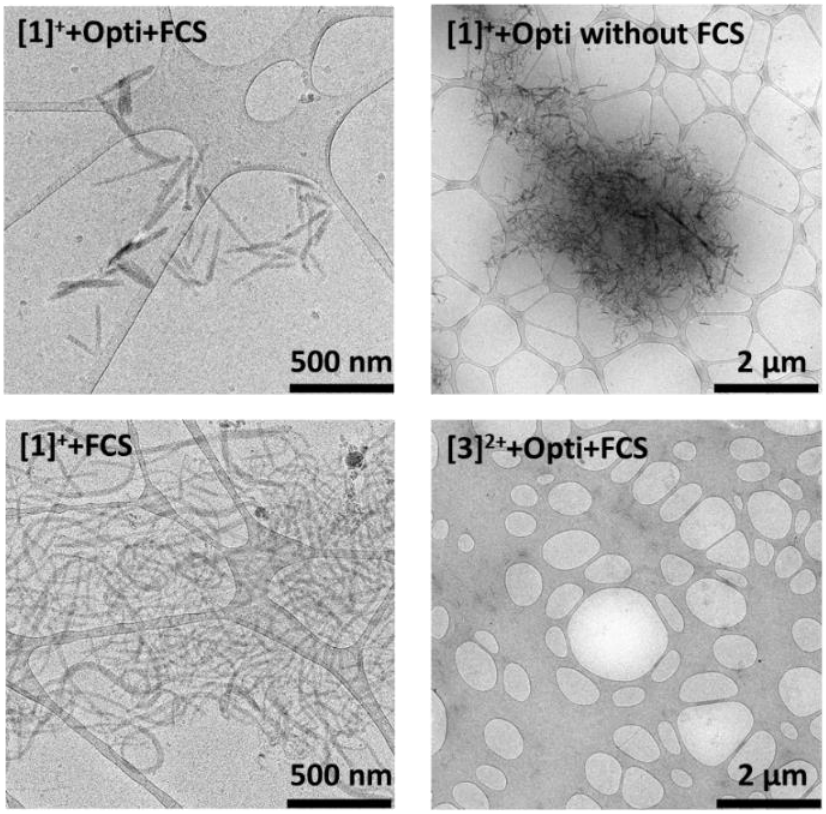

Figure 3.5 *Cryo-TEM images of complexes* ***[1]OAc*** *and* ***[3](OAc)$_2$*** *(50 µM) in Opti-MEM medium with or without FCS or pure FCS solution.*

3.2.6 Influence of the charge on the supramolecular interaction. In order to understand why **[1]**$^{+}$ and **[2]**$^{+}$ self-assemble and not **[3]**$^{2+}$, we first minimized by DFT at the PBE0/TZP/COSMO level in water a supramolecular dimer of **[1]**$^{+}$ and **[2]**$^{+}$ (Figure AII.10, Table AII.6). Minimization converged with a local minimum characterized by Pd…Pd distances of 3.18 and 3.20 Å, respectively, which qualitatively fits the experimental distance observed in the crystal structure (3.35 Å and 3.27 Å, respectively; see Figure 3.1b). This minimum demonstrates that for two isolated molecules of cyclometalated, monocationic complex **[1]**$^{+}$ or **[2]**$^{+}$, electrostatic repulsion is low enough to be compensated for the metallophilic Pd…Pd interaction, coupled to π-π stacking of the flat polyaromatic ligands. By contrast, a similar minimization run from a dimer of **[3]**$^{2+}$, assembled by hand at a short (3.18 Å) Pd…Pd distance, saw the Pd…Pd distance increase steadily to > 6.5 Å during the energy minimization, without converging (*data not shown*). This result demonstrated that for **[3]**$^{2+}$ the charge and hence the intermolecular electrostatic repulsion are too high to be compensated for the metallophilic interaction and the π-π stacking that may occur at short Pd…Pd distances. Thus, the supramolecular assembly of **[1]**$^{+}$ and **[2]**$^{+}$ seems to be modulated by the environment of the complex in solution (solvent, counteranions, and the presence of proteins), but it is an inherent property of these cyclometalated metal complexes. It originates from the strong and attractive combination between the metallophilic interaction and π-π stacking between the ligands at short Pd…Pd distances, combined with low electrostatic repulsion. For **[3]**$^{2+}$, the latter is too strong to lead to supramolecular assembly.

3.2.7 Photophysical and photochemical properties of [1]OAc in Opti-MEM complete medium. As in a cell cytotoxicity assay, the cyclometalated complexes will be added in Opti-MEM complete medium and not in water or methanol, and they will form aggregates rather than monomers. It is hence important to determine whether aggregation modifies the photophysical and photochemical properties of **[1]OAc**, compared to the monomer. The absorbance (Figure AII.11) of **[1]OAc** in the medium, for example, showed on top of a broader and more intense absorption band between 350 and 500 nm, a baseline increasing with decreasing wavelengths, which is typical for light scattering by nanoaggregates. Blue light absorption was enhanced for the aggregates compared to that for the monomer. The weak emission peak at 593 nm for **[1]OAc** in water (Figure AII.11) was quenched in Opti-MEM complete medium and replaced by a new stronger peak with a maximum at 469 nm. This new peak was located in a similar region compared to the emission peak of Opti-MEM complete medium itself, but it was more intense. The exact nature of the emitters responsible for this new

band remains unknown; in particular, it is unclear whether this peak might be attributed to supramolecular associations between **[1]OAc** and endogenous fluorophores in the medium. All in all, the emission properties of the supramolecular aggregates of **[1]OAc** were still too low to be observed *in vitro* by emission microscopy.

In terms of the $^1O_2$ generation quantum yield (φ_Δ), direct spectroscopic detection of the 1270 nm emission of $^1O_2$, which was used for determining φ_Δ of the monomer in CD_3OD, could not be used in nondeuterated aqueous cell-growing medium, where the intensity of this NIR emission band was too low. Hence, to determine the value of φ_Δ of aggregates of **[1]OAc** in Opti-MEM medium, a specific water-soluble $^1O_2$ probe was used (*i.e.*, 9,10-anthracenediyl-bis(methylene)dimalonic acid (ABMDMA). In the dark, this dye absorbs light at around 378 nm, but in presence of photogenerated $^1O_2$, it forms an endoperoxide that leads to a loss of conjugation and thus a decrease in the absorbance at 378 nm.[51] When **[1]OAc** (50 µM) was mixed with ABMDMA (100 µM) in Opti-MEM complete, the absorbance remained stable in the dark; however, upon 450 nm light irradiation the absorbance of ABMDMA dramatically decreased (Figure 3.6), showing the good $^1O_2$ production of the aggregates of **[1]OAc**. A high quantum yield of 0.73 was obtained by a quantitative comparison of the slope obtained with **[1]OAc** with the slope obtained with a reference sample of **[Ru(bpy)$_3$]Cl$_2$** (50 µM, $\varphi_{\Delta ref} = 0.14$, see Figure AII.12 and details in Appendix II).[52] Overall, **[1]OAc** restains excellent $^1O_2$ generation properties in the aggregated state and its blue light absorption properties are enhanced (*i.e.*, its blue light PDT properties are improved in cell growing medium).

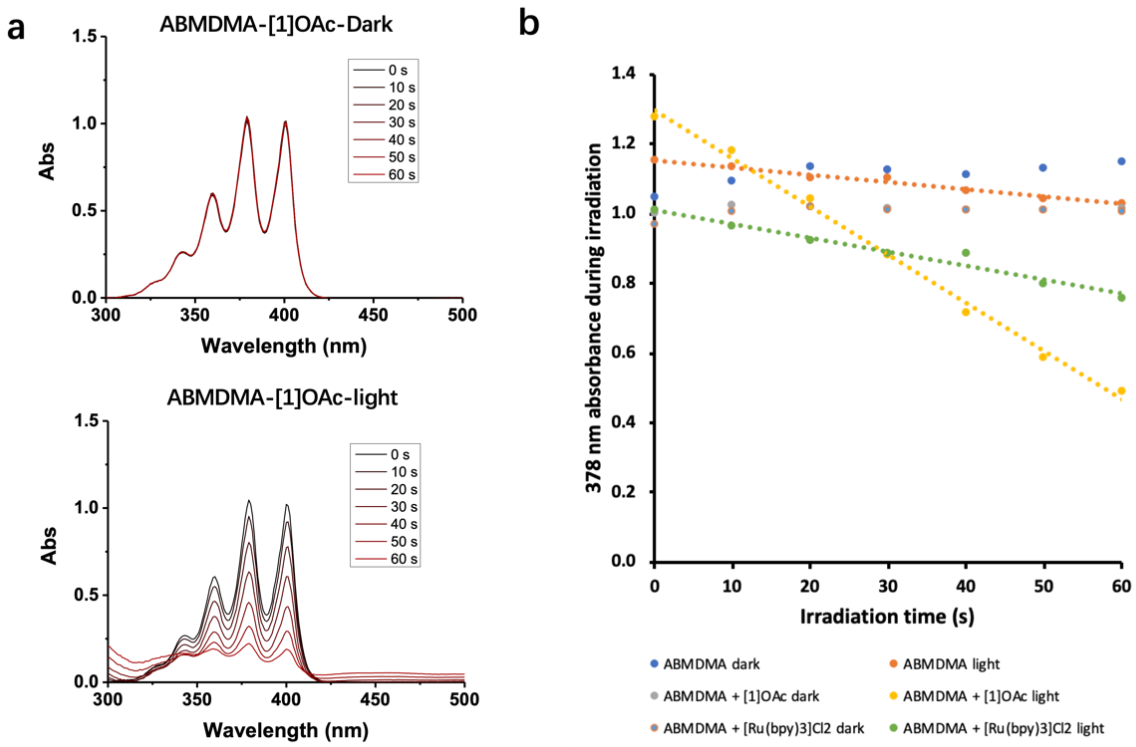

Figure 3.6 *Singlet oxygen generation of aggregates of* ***[1]OAc*** *in Opti-MEM complete medium. (a) The absorbance change of ABMDMA (100 µM) in Opti-MEM complete in the presence of* ***[1]OAc*** *(50 µM) in the dark (top) or upon blue light irradiation (bottom). (b) Evolution of the absorbance at 378 nm vs irradiation time of ABMDMA (100 µM) in Opti-MEM complete medium in the absence or presence of* ***[1]OAc*** *(50 µM) or* ***[Ru(bpy)$_3$]Cl$_2$*** *(50 µM) in the dark or under blue light irradiation. Irradiation conditions: 298 K, 450 nm, 5.23 mW cm^{-2}, and 1 min.*

3.2.8 Phototoxicity assay in normoxic and hypoxic conditions. Considering the good photodynamic properties of **[1]**$^{+}$ under blue light irradiation and its FCS-stabilized nanoaggregation behavior, the anticancer activities of **[1]**$^{+}$**-[3]**$^{2+}$ were studied first in vitro, both in the dark and following a low dose of blue light (1.7 J cm^{-2}). A dose-response curve was obtained in two human cancer cell lines A549 (lung cancer) and A431 (skin cancer) grown in 2D under normoxia (21% O_2) and using FCS-containing medium. The sulforhodamine B (SRB) assay was used as an end-point assay to quantify cell viability in treated vs untreated wells, and cisplatin was used as the positive control. The half-maximal effective concentrations (EC_{50}), defined as the compound concentration necessary to divide cell growth by a factor of 2, compared to untreated wells, and the photoindexes (PI), defined as $EC_{50,dark}/EC_{50,light}$, are reported in Table 3.3 In A549 all three complexes showed significant anticancer abilities in the

dark (EC_{50} < 10 µM), comparable to that of cisplatin, while in A431 **[3]$^{2+}$** was much more toxic than **[1]$^{+}$-[2]$^{+}$**. This result suggests that the cyclopalladated complexes, unlike **[3]$^{2+}$**, might have a form of cell toxicity in the dark that is cell-specific. Upon blue light irradiation, complex **[1]$^{+}$** showed a 6.7- and 9.4-fold increase in cytotoxicity toward A549 and A431 cancer cells, respectively, to reach 330 nM cytotoxicity for A549 cells, which is 9.4 more toxic than cisplatin (3.1 µM in dark). These results are in line with the excellent singlet oxygen generation properties of this compound under blue light irradiation, and they were comparable, at such low doses of light (< 2 J.cm^{-2}), to the photoindex obtained with the clinically approved 5-ALA control (PI = 9.8 in normoxic A431 cells, see Table 3). Meanwhile, compounds **[2]$^{+}$**-[**3]$^{2+}$** did not show any significant photocytotoxicity, which is consistent with their very low blue light absorption.

The excellent singlet oxygen generation properties of **[1]OAc** in both monomeric and aggregated forms and its clear blue light activation in normoxic cells suggested that this compound may work via a type II PDT mechanism (*i.e.*, via energy transfer from the ^{3}ILCT states of the complex to $^{3}O_2$). When the cytotoxicity experiment was repeated in the same cancer cells grown under hypoxia (1% O_2, Figure AII.13-15), the phototoxicity of **[1]$^{+}$** indeed showed a 3-fold decrease. However, it was not fully quenched, because the photoindexes of 4.6 and 6.7 in A549 and A431, respectively, were smaller compared to 6.7 and 9.4 under only normoxia, but far from unity. By contrast, two well-known PDT type II photosensitizers, 5-ALA and rose bengal, when used as the positive control, showed good PDT effect (PI<10) under normoxic conditions but no phototoxicity at all under hypoxic conditions, as expected for PDT type II photosensitizers. These results suggest that PDT type I may also occur with **[1]$^{+}$**, as observed with other metal-based sensitizers.[14] Finally, the higher EC_{50} obtained in the dark for **[1]$^{+}$-[3]$^{2+}$** under hypoxic conditions can be rationalized by the different microenvironments and gene expression usually found in hypoxic cancer cells, which are known to overexpress resistance mechanisms compared to normoxic cells.

Table 3.3 *Half maximal effective concentrations (EC_{50} in µM) of* ***[1]$^{+}$-[3]$^{2+}$****, cisplatin, 5-ALA and Rose bengal for A549 and A431 cancer cells in the dark and under blue light irradiation in normoxic (21% O_2) and hypoxic (1% O_2) conditions. 95% confidence interval (CI in µM) and photoindexes (PI = $EC_{50,dark}/EC_{50,light}$) are also indicated.*

Complex		**EC_{50} (µM)**							
		Normoxic condition				**Hypoxic condition**			
		A549	±CI	A431	±CI	A549	±CI	A431	±CI
[1]$^{+}$	Dark	2.2	+0.4	45	+13	6	+3	100	+70

			-0.4		-9		-2		-28
	Light	0.33	+0.15 -0.11	4.8	+0.9 -0.8	1.3	+0.3 -0.3	15	+2 -2
PI		6.7		9.4		4.6		6.7	
[2]$^{+}$	Dark	2.7	+0.7 -0.6	12	+4 -3	4	+1 -1	29	+38 -13
	Light	2.5	+0.7 -0.6	7	+2 -1	3	0.9 -0.8	22	+18 -8
PI		1.1		1.4		1.3		1.3	
[3]$^{2+}$	Dark	5	+2 -2	7	+2 -2	23	+8 -5	21	+2 -1
	Light	4.4	+0.9 -0.9	6	+1 -1	15	+4 -3	21	+3 -3
PI		1.1		1.2		1.5		1.0	
cisplatin	Dark	3.1	+0.6 -0.5	2.5	+0.4 -0.4	24	+11 -5	13	+4 -3
	Light	3.9	+0.8 -0.7	2.9	+0.5 -0.4	20	+8 -4	8	+2 -2
PI		0.79		0.86		1.2		1.6	
5-ALA	Dark	390	+620 -270	11000	+2200 -1900	13300	+3400 -2700	16800	+2800 -2400
	Light	170	+250 -110	1200	+1900 -850	14400	+3500 -2900	19200	+4500 -3700
PI		2.3		9.2		0.9		0.9	
Rose bengal	Dark	63	+13 -11	57	+28 -18	76	+18 -16	70	+22 -21
	Light	21	+6 -4	8	+1 -1	81	+24 -19	74	+20 -19
PI		3.0		7.1		0.9		0.9	

[a] Irradiation condition: normoxic 455 nm, 5 minutes, 5.66 mW cm^{-2}, 1.7 J cm^{-2}; hypoxic 455 nm, 8 min, 3.54 mW cm^{-2}, 1.7 J cm^{-2}. Data is the mean of three independent biological experiments.

3.2.9 Cellular uptake, subcellular fractionation, and uptake inhibition studies with A549 cells. Usually, nanoaggregates are taken up by endocytosis and end up either in the endosome or lysosome.[53] In order to check this hypothesis, A549 cells were first treated for 1 h with sodium azide (15.4 mM) or dynasore (80 μM), which inhibited active uptake and dynamin-dependent endocytosis, respectively.[54] Then, the cells were incubated with the three palladium complexes (5 μM) for a short time (*i.e.*, 3 h). The Pd contents of the cells were finally determined by ICP-MS. As shown in Figure 3.7a, in the control group without any inhibitors drug uptake of cyclometalated compounds **[1]$^{+}$-[2]$^{+}$** was 3 times higher than that of tetrapyridyl analogue [**3**]$^{2+}$. In addition, samples pretreated with NaN_3 or dynasore showed significant inhibition efficiency for the uptake of **[1]$^{+}$-[2]$^{+}$**, while no inhibition was observed for **[3]$^{2+}$**. These results demonstrated that **[1]$^{+}$-[2]$^{+}$** were taken up in the cell via active, dynamin-

dependent endocytosis, while **[3]$^{2+}$** went into the cells by energy-independent uptake, possibly passive diffusion. This assay confirmed that **[1]$^{+}$-[2]$^{+}$** entered the cells as nanoaggregates and that cyclometalation dramatically changed the mechanism of cellular uptake.

In a second experiment aimed at determining the intracellular localization, at longer incubation times for these nonemissive palladium complexes, A549 cells were treated with complexes **[1]OAc-[3](OAc)$_2$** (1 μM) for 24 h and then trypsinized and fractionated into four fractions: cytosol, membranes, nuclei, and cytoskeleton. The membrane fractions include not only the cell membrane, but also the membranes in the mitochondria, endosomes, and lysosomes. In principle, nanoaggregates of **[1]$^{+}$-[2]$^{+}$** were expected to end up in the membrane fraction. The results (Figure 3.7b, Table AII.7) did not fit such expectations. **[1]$^{+}$-[2]$^{+}$** were found neither in the membrane nor in the nuclear fractions, but almost exclusively (94.3% and 89.1%, respectively) in the cytoskeleton fraction. In contrast, **[3]$^{2+}$** was distributed among the cytoskeleton (61.1%), the membrane fraction (15.5%), and the cytosol (23.3%). Besides, as at shorter times the total amount of palladium found in the cells was more than 10 times higher for cyclometalated complexes **[1]$^{+}$-[2]$^{+}$** (19 and 14 ng Pd/million cells, respectively) than for **[3]$^{2+}$** (1.7 ng Pd/million cells). Overall, these combined ICP-MS results confirmed previous reports that cyclometalated compounds are more efficiently taken up than their polypyridyl analogue. However, they also shed new light on the reason for such enhanced uptake: considering their similar log P_{ow} values but very different aggregation behavior in the FCS-containing cell medium, it is the nanoaggregation of cyclometalated compounds **[1]$^{+}$-[2]$^{+}$**, stabilized by FCS, that leads to enhanced cellular uptake, rather than passive uptake by diffusion through the cell membrane. In addition, the supramolecular nature of the interactions leading to aggregate formation seems weak enough to allow for a redistribution of the palladium complex after endocytosis, as palladium ends up in the cytoskeleton fraction, rather than in the endosome or lysosome. According to this study, the mode of action of [**1**]$^{+}$-[**2**]$^{+}$ is very unlikely to be related to nuclear DNA damage, suggesting that these compounds may overcome chemotherapy resistance originating from DNA damage repair.

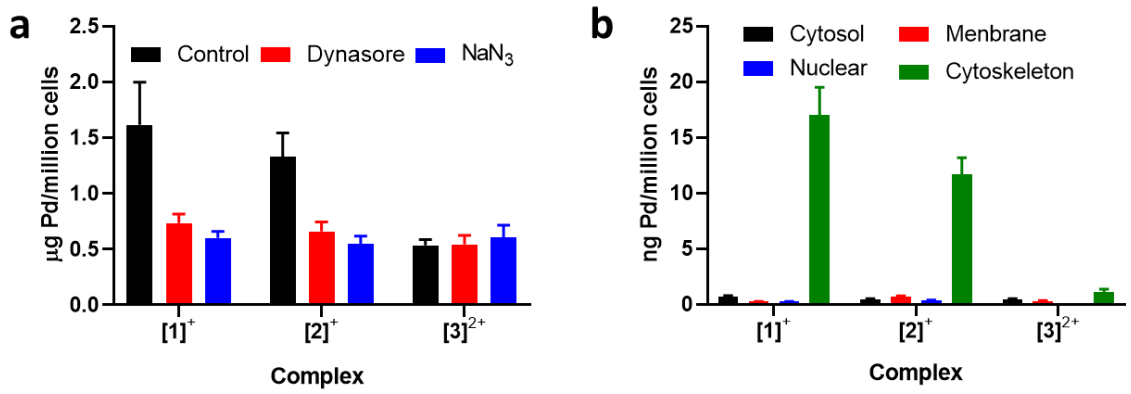

Figure 3.7 *(a) Pd contents (expressed in µg Pd/million cells) of A549 cells after treatment with NaN_3 or dynasore for 1 h and compounds* ***[1]$^+$-[3]$^{2+}$*** *(**5** µM) for 3 h. (b) Distribution (expressed in ng Pd/million cells) of palladium compounds* ***[1]$^+$-[3]$^{2+}$*** *in the cytosol (black), membranes (red), nucleus (blue), and cytoskeleton (green) of A549 cells after treatment at 1 µM for 24 h.*

3.2.10 Intracellular ROS determination and apoptosis. The generation of ROS in cancer cells usually induced cell death via apoptosis.[55] 2,7-Dichlorodihydrofluorescein diacetate (DCFH-DA) is an excellent sensor for intracellular ROS, which generates green-emissive metabolite dichlorofluorescein (DCF). ROS levels were hence measured in A549 cells using flow cytometry after treatment with **[1]$^+$-[3]$^{2+}$** (5 µM) followed or not by blue light irradiation (455 nm, 5 min, 5.66 mW cm^{-2}, 1.7 J cm^{-2}, Figure 3.8a). In the dark, cyclometalated complexes **[1]$^+$-[2]$^+$** showed significant ROS levels, even higher than that for the positive control (400 µM H_2O_2). Upon 455 nm irradiation, the ROS levels in all groups increased, especially for complex **[1]$^+$**, with a 3.5-fold enhancement and the highest ROS level of all samples. This experiment confirmed the photodynamic character of light-induced cell killing with **[1]$^+$**. The ROS level found for **[2]$^+$** under blue light irradiation was close to the sum of the ROS levels found in cells treated with only blue light and that of cells treated with **[2]$^+$** and left in the dark, indicating the weak light-induced ROS generation ability of complex **[2]$^+$**. Unexpectedly, **[3]$^{2+}$** inhibited ROS generation, compared with cells treated with **[3]$^{2+}$** but kept in the dark or cells irradiated with blue light in the absence of any compound. The cytotoxicity difference between cyclometalated complexes **[1]$^+$-2$^+$** and **[3]$^{2+}$** is the ability of the former to generate ROS in the dark, and the ability of **[1]$^+$** to absorb blue light to increase ROS generation.

The cell death mode triggered by such ROS formation in A549 cells was determined by flow cytometry using the Annexin V-FITC/propidium iodide double staining assay (Figure AII.16). After 24 h of incubation with each complex, the A549 cells were irradiated with blue light or left in the dark and incubated for another 24 h and then harvested and treated with both dyes

for FACS analysis. The percentage of live cells (Annexin -, PI -), early apoptotic (Annexin +, PI -), later apoptotic (Annexin +, PI +), and necrotic (Annexin -, PI +) cells, are shown in Figure 8b. Clearly, in the dark **[1]**$^{+}$**-[3]**$^{2+}$ provoke cell death via apoptosis. Under blue light irradiation, the percentage of apoptotic cells induced by complex **[1]**$^{+}$ increased by 21% (from 71 to 92%), while the other two complexes increased by only 4.3% (**[2]**$^{+}$) and 7.1% (**[3]**$^{2+}$). Overall, in A549 cells **[1]**$^{+}$ kills cells via apoptosis in the dark by generating ROS near the cytoskeleton; this action is dramatically enhanced by low doses of blue light irradiation.

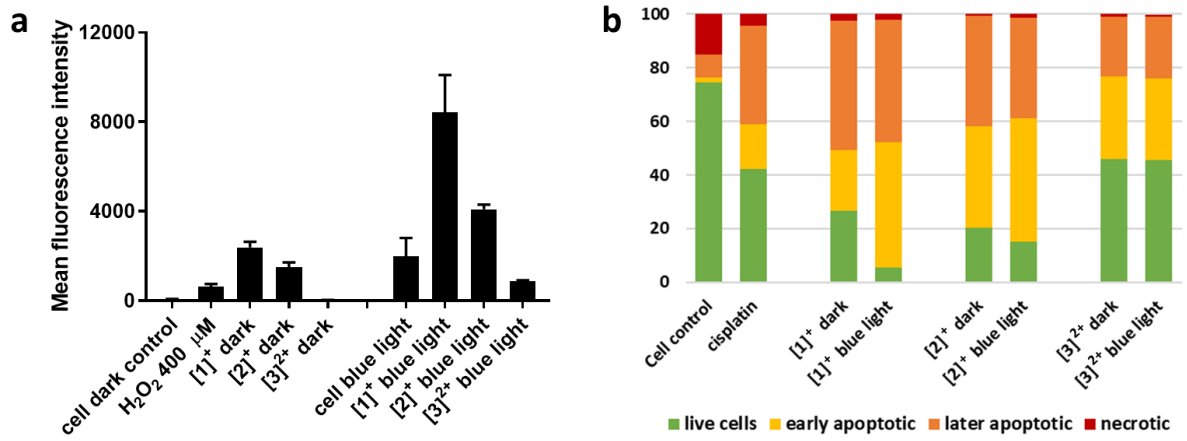

Figure 3.8 *(a) Mean fluorescence intensity of cells treated first with* ***[1]OAc-[3](OAc)***$_2$ *(5 µM, 24 h) and then with DCFDA (20 µM, 30 min), and analyzed by flow cytometry; (b) Flow cytometry quantification of alive (Annexin -, PI -), early apoptotic (Annexin +, PI -), later apoptotic (Annexin +, PI +), and necrotic (Annexin -, PI +) A549 cells after treatment with* ***[1]***$^{+}$***-[3]***$^{2+}$ *(15 µM) or cisplatin (15 µM) in the dark or after irradiation for 5 min with blue light (455 nm, 5.66 mW cm*$^{-2}$*, 1.7 J cm*$^{-2}$*).*

3.2.11 Photocytotoxicty of [1]OAc in 3D tumor spheroids. In 2D cell monolayers, the physical access of the drug to the cancer cells is not an issue and light optimally and equally bathes all cells, which represents a poor model of in vivo tumor treatment with PDT. By contrast, 3D multicellular tumor spheroid models provide a more accurate biological evaluation of the physical penetration of PDT drugs, nanoparticle-based drug delivery systems, and light.[56] The cytotoxicity of **[1]**$^{+}$ in FCS-containing medium was hence tested in 3D tumor spheroids using a CellTiter-Glo 3D cell viability end-point assay to quantify the ATP concentration.[57] As shown in Figure 3.9, it was possible to fully eradicate the tumor spheroids in the dark, suggesting that the nanoaggregates of **[1]**$^{+}$ and FCS either well penetrated the spheroid to kill simultaneously all cell layers including the center, or destroyed the outer layers of the spheroids first to move toward the center and kill the cells there. Upon blue light activation (455 nm, 10 min, 3.48 mW

cm^{-2}, 2.1 J cm^{-2}) the EC_{50} value of 3D tumor spheroids decreased by 6.2-fold, from 13 to 2.1 µM, and here as well full eradication of ATP production could be achieved. Such a photoindex is surprisingly similar to the one measured in normoxic 2D cell monolayers (6.7), which again suggests that sensitizer penetration is not an issue here. These results not only confirm the excellent potential of **[1]**$^+$ as a blue light PDT agent, but also highlight its ability to penetrate, as a nanoaggregate, to the core of tumor spheroids, and to kill all cancer cells by a combination of a chemical (dark toxicity) and photochemical (blue-light activation) effect.

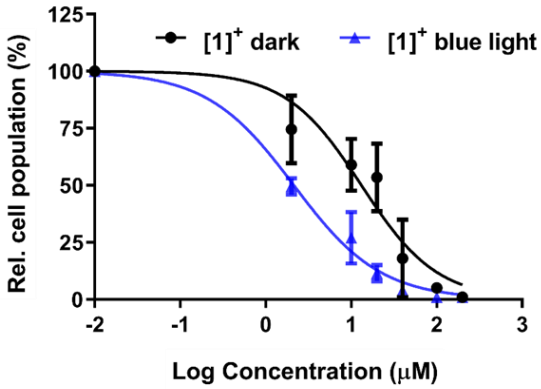

Figure 3.9 *Dose-response curves for A549 3D tumor spheroids incubated with complex* ***[1]***$^+$ *irradiated for 10 min with blue light (in blue) or kept in the dark (in black).* $EC_{50,dark}$ *= 13 µM (95% confidence intervals +7.7 µM, -6.0 µM),* $EC_{50,light}$ *= 2.1 µM (95% confidence intervals +0.7 µM, - 0.7 µM), PI = 6.2.*

3.2.12 ***In vivo*** **experiments.** The penetration of blue light well matches the depth of skin cancers in the human body. Considering the excellent dark cytotoxicity of **[1]OAc** *in vitro* and its good photodynamic properties in hypoxic cancer cells and 3D tumor spheroids, the *in vivo* antitumor property of compound **[1]OAc** was evaluated, in the dark or upon blue light irradiation (450 nm), in 4T1 breast tumor xenografts in Balb/c female mice. This model is a commonly used subcutaneous tumor model in mice, which is better suited for blue light PDT *in vivo* than orthotopic xenografts models because of the short irradiation wavelength used. In general, intravenous tail injection is the main injection method for in vivo antitumor experiments because it best mimics the mode of administration of PDT sensitizers in clinical trials. However, in this work the higher dark cytotoxicity of the palladium complexes, compared to clinically approved PDT sensitizers, led us to consider paracancerous injection and a short drug-to-light interval of 1 h as a more efficient method for maximizing the drug concentration near the tumor and hence the PDT effect, while minimizing toxicity to the mice. Compound **[2]OAc** was also tested as a control complex that also forms nanoparticles in the presence of proteins, but does

not absorb blue light at that wavelength. The mice (N=3) were divided into six groups when the tumor volume reached around 40 mm^3: dark vehicle control, blue light-irradiated vehicle control, and injection of **[1]OAc** or **[2]OAc** (40 µM, 100 µL) either with or without blue light irradiation in a 60 J cm^{-2} light dose. The mice were treated twice, at days 0 and day 2. One hour after compound injection, the mice were irradiated with blue light for 20 min. The tumor volume of each mouse (Figure 3.10a), and the body weight (Figure AII.17) were measured and recorded over 10 days following treatment. On day 10, the mice were sacrificed, and tumors were isolated to compare the volume scale of tumor spheres. All mice showed similar body weight at the end of the treatment (around 20 g), meaning that the mice were healthy and the complexes were not very toxic to the mice themselves. At day 10, the tumor of dark vehicle control and blue light-irradiated vehicle control groups showed similar (and highest) volumes, followed by the mice group treated with **[2]**$^+$ (dark) > **[2]**$^+$ (450 nm) > **[1]**$^+$ (dark) > **[1]**$^+$ (450 nm). In the dark, the tumor volumes of mice were gradually growing with the treatment of complex **[1]**$^+$ and **[2]**$^+$ from day 0 to day 8 and then significantly increased on day 10. When treated with **[1]**$^+$ and irradiated with blue light on days 0 and 2, no obvious growth of the tumor occurred over 10 days (Figure 3.10a), demonstrating the excellent photodynamic therapy properties of **[1]**$^+$ under these conditions.

As a side note, when the intravenous tail injection of a PDT sensitizer is chosen, longer drug-to-light intervals are typically used (4-24 h) in order to wait for the PDT sensitizer to accumulate in the tumor, in particular, for sensitizer nanoformulations relying on the enhanced permeability and retention (EPR) effect to enter the tumor. By contrast, paracancerous injection is a quicker and more direct method of concentrating the sensitizer (here the Pd nanoaggregates) near the tumor site. Also, it is better than intratumoral injection because paracancerous injection still holds the possibility of blood circulation of the drug to occur. On the other hand, a longer drug-to-light interval could lead to further transport of the drug to the rest of the body and unwanted toxicity to occur. Thus, a rather short drug-to-light time of 1 h was chosen. The final results suggest that 1 h is indeed a reasonable time setting and that under such conditions **[1]**$^+$ penetrates well enough into the tumor to serve as a PDT sensitizer.

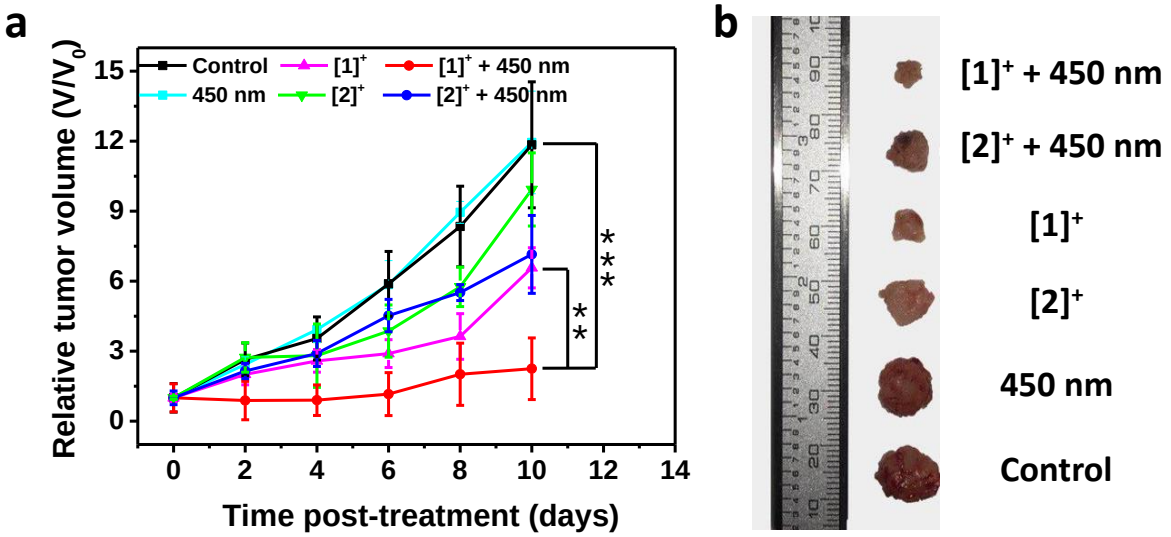

Figure 3.10 *(a) Relative 4T1 breast tumor volumes of Balb/c mice and (b) visual tumor sizes at day 10 of Balb/c mice treated with vehicle control,* ***[1]***$^{+}$*, or* ***[2]***$^{+}$ *at day 0 and left in the dark or irradiated with blue light. Mice were treated on days 0 and 2 and irradiated with blue light (450 nm, 50 mW cm*^{2}*, 20 min, 60 J cm*$^{-2}$*) 1 h after injection. Statistical significance was set to p < 0.01 (**) and 0.001 (***).*

3.3 Discussion

Traditionally, a vast majority of the PDT literature argues that because light penetration is better with red light than with blue light, blue light PDT is not relevant *in vivo*. Recently, however, research compared blue light *vs.* red light for the 5-aminolevulinic acid (ALA) photodynamic therapy of basal cell carcinoma patients.[58, 59] 5-ALA is transformed selectively by tumors into protoporphyrin IX, which can be excited either in the Soret band using blue light or in the Q band using red light. In this study, blue light showed statistically noninferior efficacy compared to red light, and a lower light fluence rate could be used with blue light due to the better light absorption of the Soret band, which generated less pain for the patients.[58] These results suggested that blue light PDT should be studied and optimized further to evaluate its potential as an effective nonscarring anticancer treatment option in, for example skin, eye, or bladder cancer. In cancers of superficial tissues indeed, short-wavelength (blue or green) PDT agents are interesting because short-wavelength light potentially reduces the damage to deeper healthy tissues. For skin cancer, for example, skin contains two layers: the cuticular layer (~0.08-0.27 mm thickness) and the derma (~2.1-5.9 mm thickness).[60] As in skin tissue the penetration depth for blue, red, and NIR light is 1-2 mm, 4-5 mm, and > 5 mm, respectively,[61] hence blue light may reduce photodynamic damage to the derma. It is known that the cuticular tissue can recover

soon after damage, but for the derma, tissue recovery is sometimes difficult. Thus, in the treatment of skin diseases, it is beneficial to reduce damage to the derma. Similar strategies are being developed in bladder cancer patients, where the green light PDT sensitizer (TLD1433) is currently in clinical phase II trial[13], to alleviate the phototoxicity issues experienced with red light PDT using photofrin at the end of the 1990s.[62] Recently, Lilge's group reported a method to formulate TLD1433 with transferrin, which improved molar extinction coefficients in the visible domain of the spectrum, ROS production by the photosensitizer, cellular uptake, and the in vivo PDT efficacy.[63] These results provide an inspiring example of how to further improve the photoactivity of cyclometalated PDT compounds such as **[1]**$^{+}$.

In the present study, **[1]**$^{+}$ stands out for two reasons. First, it is an excellent singlet oxygen generator under blue light irradiation, while **[2]**$^{+}$ and **[3]**$^{2+}$ have negligible absorption and singlet oxygen generation properties at such wavelengths. The bathochromically shifted absorbance of **[1]**$^{+}$ is a consequence of the lower HOMO-LUMO gap in this compound due to (i) the presence and (ii) the position of the Pd-C bond with respect to the noncoordinated amine bridge.[36] The photodynamic properties of **[1]**$^{+}$ were observed in both normoxic and hypoxic 2D cell monolayers, suggesting that **[1]**$^{+}$ can serve for both PDT type II (normoxia) and type I (hypoxia). Second, the self-aggregation properties of **[1]**$^{+}$ and **[2]**$^{+}$ cause them efficiently penetrate into cancer cells via endocytosis where it is distributed to the cytoskeleton, while **[3]**$^{2+}$ is taken up in smaller amounts and codistributed in the membranes and cytosol. These self-assembly properties are a direct consequence of the lower charge of the cyclometalated complexes, of their extended, flat aromatic ligand, of the presence of a palladium(II) atom in the center of the complexes, which generates Pd…Pd metallophilic interaction,[43, 64, 65] and of the stabilization of the self-assembled nanorods in a biological medium by serum proteins. One should also note that although aggregation is often detrimental to the photodynamic properties of porphyrin sensitizers for example, with cyclometalated palladium compounds such as **[1]**$^{+}$ self-assembly leads to nanostructures without quenching the blue-light photoreactivity. Of course, aggregation of the Pd complex as nanorods in the cell medium suggests that aggregation may also occur in the blood, and that sensitizer uptake by the tumor may partially rely on the enhanced permeability and retention (EPR) effect via the trans-endothelial pathways. However, at that stage these hypotheses remain speculations. Altogether, the excellent uptake, localization, and photodynamic properties of **[1]**$^{+}$ make it an interesting blue-light-activated tumor killer not only in the 3D spheroid model, but also in 4T1 breast tumor xenografts in mice.

3.4 Conclusion

For metal-based anticancer drugs and photosensitizers, achieving cytotoxicity requires efficient cellular uptake. The most common method for increasing cellular uptake, which consists of increasing the lipophilicity of the compounds, allows for a better crossing of the lipophilic phospholipid bilayer of cells. Cyclometalation is one way to enhance the lipophilicity of metal complexes, and it almost systematically significantly improves cellular uptake. On the other hand, such a strategy is usually detrimental to the selectivity of the uptake, because healthy cells also have a membrane, too. Our work offers a new perspective on the effects of cyclometalation on cell uptake beyond a simple increase in molecular lipophilicity. First, the octanol-water partition coefficient (log P) is always measured in the absence of serum protein, so similar log P values do not necessarily allow for predicting the solubility and aggregation properties of a drug candidate in cell growing medium or blood. Second, when the balance between hydrophobicity and self-assembly properties is just right, cyclometalated complexes such as palladium complexes **[1]**$^{+}$ and **[2]**$^{+}$ can generate nanoaggregates. Our results unambiguously demonstrate that the colloidal stability of these aggregates critically depends on the presence of the protein component (FCS) of the cell-growth medium and that in the presence of serum, cellular uptake *in vitro* is greatly enhanced, compared to that of nonaggregated compounds such as **[3]**$^{2+}$. Endocytosis probably plays a critical role here; however, it should be noted that the compound was finally detected in the cytoskeleton rather than in the endosome or lysosome, which suggests that the supramolecular nature of the interaction responsible for the aggregation (*i.e.*, Pd…Pd metallophilic interaction) may be reversible in the cell and allow for the compound to escape the endocytic pathway. Protein-controlled self-assembly in aqueous solution via Pd…Pd metallophilic interaction has not been documented before. It suggests that (pro)drug self-assembly in serum may offer straightforward strategies for improving drug uptake without a sophisticated drug delivery system and that such strategies may work not only *in vitro*, but also *in vivo*.

3.5 Experimental Section

3.5.1 Compounds preparations. The starting materials and precursors **HL^{1}-HL^{3}** were prepared according to literature methods.[36] The preparation details of ligands **MeL^{1}**, **MeL^{2}**, and **MeL^{3}** and corresponding metal complexes **[PdMeL^{1}]OAc ([1]$^{+}$)**, **[PdMeL^{2}]OAc ([2]$^{+}$)**, and **[PdMeL^{3}](OAc)$_2$ ([3]$^{2+}$)** are given in the below. All solvents and reagents were purchased from commercial vendors and used without purification. All synthesis was performed in a dinitrogen atmosphere. The metal complexes were synthesized and purified without column

chromatography in high yields. In the subsequent report, the complexes are all in the CH_3COO^- counterion unless otherwise specified.

3.5.1.1 Synthesis of ligand MeL[1], MeL[2], and MeL[3]

The three ligands were synthesized in the same reaction conditions. The synthesis of **MeL[1]** is described in detail below as an example.

MeL[1]

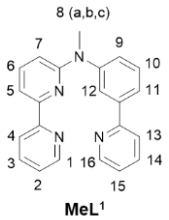

MeL[1]

A mixture of its precursor **HL[1]** (324.0 mg, 1.0 mmol), KOtBu (448.4 mg, 2.0 mmol), and CH_3I (282.0 mg, 0.1 mL, 2.0 mmol), was dissolved in DMF (10 mL) and stirred for 24 h at room temperature under an N_2 atmosphere. Then the reaction solution was extracted with ethyl acetate (EtOAc) and water. NH_4Cl was add to the extracting solution for a good separation of the two layers. The crude product collected from the EtOAc layer was purified by silica gel chromatography using Pentane:EtOAc 4:1 (R_f = 0.25) to 2:1 (R_f = 0.35) as eluents. MeL[1] was obtained in 47% yield (159.0 mg, 0.47 mmol). **ESI-MS** (cation): m/z calcd 339.2 ($C_{22}H_{18}N_4 + H^+$), obsd 339.2; **^{1}H NMR** (400 MHz, Methanol-*d*$_4$) δ 8.58 (2 H, dddd, J = 9.6, 4.9, 1.8, 0.9 Hz, H^1, H^{12}), 8.39 (1 H, dq, J = 8.0, 0.9 Hz, H^4), 7.92 (1 H, t, J = 2.0 Hz, H^{15}), 7.90 – 7.82 (3 H, m, H^{16}, H^3, H^{14}), 7.80 (1 H, ddd, J = 7.7, 1.8, 1.0 Hz, H^{13}), 7.63 (1 H, dd, J = 7.4, 0.8 Hz, H^9), 7.59 – 7.47 (2 H, m, H^6, H^{11}), 7.43 – 7.27 (3 H, m, H^2, H^5, H^{10}), 6.67 (1 H, dt, J = 8.5, 0.7 Hz, H^7), 3.61 (3 H, d, J = 0.6, H^8). **^{13}C APT-NMR** (101 MHz, Methanol-*d4*) δ 159.6, 158.3, 158.1, 154.8, 150.4, 149.7, 148.8, 142.1, 139.0, 138.9, 138.6, 131.2, 128.0, 126.0, 125.2, 124.9, 124.0, 122.7, 122.6, 111.6, 110.7, 38.8.

MeL[2]

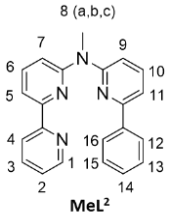

MeL[2]

This ligand were collected from the EtOAc layer was purified by silica gel chromatography using Pentane:EtOAc 4:1 (R_f = 0.25) to 2:1 (R_f = 0.35) as eluents. Yield 143.4 mg, 0.42 mmol, 42%; **ESI-MS** (cation): m/z calcd 339.2 ($C_{22}H_{18}N_4 + H^+$), obsd 339.2; **^{1}H NMR** (300 MHz, Methanol-*d*$_4$) 8.62 (1 H, d, *J* = 4.9 Hz, H^1), 8.38 (1 H, d, *J* = 8.0 Hz, H^5), 8.12 – 7.99 (2 H, m, H^{12}, H^{15}), 7.99 – 7.85 (2 H, m, H^3, H^6), 7.77 (2 H, td, *J* = 8.1, 6.8 Hz, H^4, H^{10}), 7.53 – 7.33 (6 H, m, H^{14}, H^{13}, H^{15}, H^2, H^{11}, H^7), 7.27 (1 H, d, *J* = 8.2 Hz, H^9), 3.79 (3 H, d, *J* = 1.7 Hz, H^8); **^{13}C APT-NMR** (75 MHz, Methanol-*d*$_4$) δ 149.9, 139.6, 139.3, 138.7, 128.0, 129.7, 127.8, 125.1, 122.7, 115.6, 114.9, 114.9, 114.4, 36.5.

MeL[3]

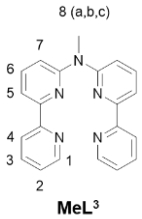

This ligand was purified by alumina column chromatography with eluent Pentane:EtOAc (20:3, R_f = 0.3). Yield 56 mg, 0.17 mmol, 97%; **ESI-MS** (cation): m/z calcd 340.2 ($C_{22}H_{18}N_4 + H^+$), obsd 340.3; **^{1}H NMR** (400 MHz, Methanol-*d*$_4$) 8.64 – 8.59 (2 H, m, H^1), 8.36 (2 H, dt, J = 8.0, 1.1 Hz, H^4), 7.94 – 7.88 (4 H, m, H^5, H^3), 7.80 (2 H, dd, J = 8.3, 7.5 Hz, H^6), 7.44 – 7.34 (4 H, m, H^2, H^7), 3.80 (3 H, s, H^8). **^{13}C APT-NMR** (101 MHz, Methanol-*d4*) δ 157.2, 156.1, 153.9, 148.6, 138.1, 137.3, 123.7, 121.2, 114.5, 113.8, 113.3, 35.0.

3.5.1.2 Synthesis of palladium complexes

[PdMeL^1]OAc ([1]OAc)

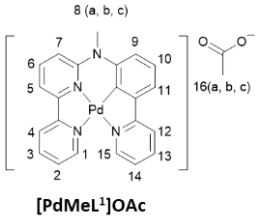

A mixture of ligand **MeL^1** (67.6 mg, 0.20 mmol) and and $Pd(OAc)_2$ (44.4 mg, 0.20 mmol) was dissolved in CH_3COOH (50 mL) and heating at 135 °C on N_2 atmosphere for 24 h. The solvent was rotary evaporated to obtain a yellow solid, which was washed with EtOAc (50 mL) and ether (30 mL), and dried under vacuum, to finally obtain **(1]OAc** as analytically pure product (Yield: 86 mg, 0.17 mmol, 86%). **HRMS** (cation): m/z calcd 443.0488 $[C_{22}H_{17}N_4Pd]^+$, obsd 443.0493. **^{1}H NMR** (300 MHz, Methanol-*d*$_4$) 8.55 (1 H, d, *J* = 5.4 Hz, H^1), 8.35 (2 H, t, *J* = 8.3 Hz, H^4, H^{15}), 8.18 (1 H, td, *J* = 8.0, 1.5 Hz, H^3), 8.05 – 7.93 (2 H, m, H^6, H^{13}), 7.88 (2 H, td, *J* = 7.4, 1.3 Hz, H^5, H^{12}), 7.69 (1 H, ddd, *J* = 7.3, 5.6, 1.2 Hz, H^2), 7.45 – 7.30 (3 H, m, H^7, H^{11}, H^{14}), 7.25 (1 H, t, *J* = 7.8 Hz, H^{10}), 7.07 (1 H, dd, *J* = 8.4, 1.0 Hz, H^9), 3.59 (3 H, s, H^8), 1.90 (3 H, s, H^{16}). **^{13}C APT-NMR** (75 MHz, Methanol-*d*$_4$) δ 150.3, 149.4, 141.6, 141.4, 140.4, 124.8, 124.8, 121.5, 120.6, 119.7, 118.3, 116.3, 42.1. Elemental analysis calcd for **[1]OAc** + 6H_2O: C, 47.18; H, 5.28; N, 9.17; Found for **[1]OAc** + 6H_2O: 47.20, 5.22, 9.35**.**

[PdMeL^2]OAc ([2]OAc)

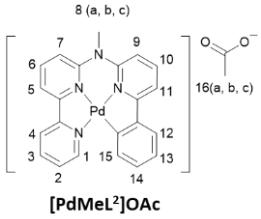

[2]OAc was synthesized using the same method as for **[2]OAc**, but starting from ligand **MeL^2** (67.6 mg, 0.2 mmol). The yield in **[2]OAc** was 88% (88.7 mg, 0.18 mmol). **HRMS** (cation): m/z calcd 443.0488 $[C_{22}H_{17}N_4Pd]^+$, obsd 443.0490. **^{1}H NMR** (400 MHz, Methanol-*d*$_4$) 8.73 (1 H, dd, J = 5.9, 1.4 Hz, H^1), 8.39 – 8.32 (1 H, m, H^4), 8.22 (1 H, td, J = 7.8, 1.5 Hz, H^3), 8.18 – 8.10 (1 H, m, H^6), 8.01 (1 H, d, J = 7.7 Hz, H^5), 7.95 (1 H, t, J = 8.1 Hz, H^{10}), 7.67 (1 H, ddd, J = 7.3, 5.6, 1.4 Hz, H^2), 7.55 (2 H, dd, J = 11.6, 8.1 Hz, H^7, H^{11}), 7.52 – 7.48 (1 H, m, H^{14}), 7.20 (1 H, d, J = 8.5 Hz, H^9), 7.17 – 7.09 (3 H, m, H^{15}, H^{13}, H^{12}), 3.61 (3 H,

s, H^8), 1.90 (3 H, s, H^{16}). **^{13}C APT-NMR** (101 MHz, Methanol-d_4) δ 165.0, 158.0, 156.5, 152.7, 152.0, 151.8, 151.1, 142.2, 141.8, 141.7, 132.1, 130.5, 128.2, 127.0, 125.8, 125.3, 118.6, 118.1, 115.0, 114.7, 43.6. Elemental analysis calcd for **[2]OAc** + $2H_2O$: C, 53.49; H, 4.49; N, 10.40; Found for **[2]OAc** + $2H_2O$: 53.46, 4.53, 10.38**.**

[PdMeL^3](OAc)$_2$ ([3](OAc)$_2$)

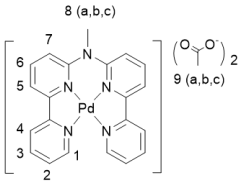

[PdMeL^3](OAc)$_2$

The mixture of ligand **MeL^3** (23.3 mg, 0.065 mmol) and $Pd(OAc)_2$ (25.6 mg, 0.065 mmol) was dissolved in MeOH and heated at 65 °C under an N_2 atmosphere for 24 h. The solvent was rotary evaporated to obtain a yellow solid, which was washed with EtOAc (50 mL) and and ether (30 mL), dried in vacuum to obtain **[3](OAc)$_2$** as analytically pure product (Yield: 29.3 mg, 0.054 mmol, 80%). **HRMS** (cation): m/z calcd 222.5254 $[C_{21}H_{17}N_5Pd]^{2+}$, obsd 222.5255. **^{1}H NMR** (400 MHz, Methanol-d_4) 9.03 (2 H, d, J = 5.8 Hz, H^1), 8.75 (2 H, d, J = 8.1 Hz, H^4), 8.52 (6 H, dt, J = 16.2, 7.5 Hz, H^3, H^5, H^6), 8.04 (4 H, dd, J = 8.3, 5.2 Hz, H^7, H^2), 4.08 (3 H, s, H^8), 1.87 (6 H, s, H^9). **^{13}C APT-NMR** (101 MHz, Methanol-d_4) δ 158.3, 155.4, 152.2, 151.2, 144.1, 143.8, 129.4, 125.9, 120.4, 119.9, 44.1. Elemental analysis calcd for **[3](OAc)$_2$** + $8H_2O$: C, 42.41; H, 5.55; N, 9.89; Found for **[3](OAc)$_2$** + $8H_2O$: 42.63, 4.92, 9.98.

3.5.2 Partition coefficients (log P_{ow}) determination. The partition coefficients of palladium complexes were determined by the shake-flask method. In brief, the palladium complexes were dissolved in octanol-saturated water and ultrasonicated for 1 h to prepare 1 mM stock solutions. After filtering with a 0.2 µM membrane filter, aliquots of the stock solutions (0.2 mL) were transferred per duplicate to 15 mL centrifuge tubes and diluted up to 1 mL using octanol-saturated water. Then, 1 mL of water-saturated octanol was added to one of the tubes and the mixtures were shaken in an IKA Vibrax shaker for 24 h at 2200 pm. The mixture was centrifuged for 20 min at 4300 rpm to separate the water phase. An aliquot of the water phase (0.4 mL) was first mixed with 0.8 mL of 65% HNO_3 and then diluted with Milli-Q water (4.8 mL) to make 8.7% HNO_3 solution (6 mL). The palladium content of these samples was determined by ICP-OES using a Vista-MPX CCD simultaneous ICP-OES. Partition coefficient log P_{ow} was calculated using the equation below,

$$\log P_{ow} = \log ([Pd]_{oct}/[Pd]_{aq}) = \log ([Pd]_{total} - [Pd]_{aq}) /[Pd]_{aq}$$

where $[Pd]_{total}$ is the concentration of palladium in the control sample (where no water-saturated octanol was added) and $[Pd]_{aq}$ is the concentration of palladium in the aqueous layer.

3.5.3 Single-crystal X-ray diffraction. The CH_3COO^- counterion of **[1]**$^+$ and **[2]**$^+$ was changed to PF_6^- ion by adding excess KPF_6 to a water solution of the acetato metal complexes, to obtain a precipitate of **[1]PF$_6$** and **[2]PF$_6$** that was filtered off and dried. The single crystals suitable for X-ray structure determination were obtained for **[1]PF$_6$** and **[2]PF$_6$** via slow evaporation of a solution of the metal complex (PF_6 counterion) in a MeCN/EtOAc mixture (2:1). Single crystals of **[3]BF$_4$** were obtained via vapor diffusion from diethyl ether to a MeCN/EtOAc solution of **[3](OAc)$_2$** containing HBF_4. All reflection intensities were measured at 110(2) K using a SuperNova diffractometer (equipped with an Atlas detector) with Mo Kα radiation (λ = 0.71073 Å) for **[1]PF$_6$** and **[3](BF$_4$)$_2$** and with Cu *K*α radiation (λ = 1.54178 Å) for **[2]PF$_6$** via the program CrysAlisPro program (Version CrysAlisPro 1.171.39.29c, Rigaku OD, 2017). The same program was used to refine the cell dimensions and reduce the data. The structure was solved with the SHELXS-2018/3 program (Sheldrick, 2018) and was refined on F^2 with SHELXL-2018/3 (Sheldrick, 2018). Numerical absorption correction based on Gaussian integration over a multifaceted crystal model was performed using CrysAlisPro. The temperature of the data collection was controlled using the Cryojet system (manufactured by Oxford Instruments). The H atoms were placed at calculated positions (unless otherwise specified) using the AFIX 43 or AFIX 137 instructions with isotropic displacement parameters having value of 1.2 or 1.5 U_{eq} for the attached C atoms. For **[2]PF$_6$**, the H atoms attached to N1 and N21 were found from different Fourier maps, and their coordinates were refined pseudofreely. The H1…H21 distance was set to be found within an acceptable range (> 1.9 Å) using the DFIX instructions.

3.5.4 Photophysical properties measurements. Absorption spectra of complexes were recorded on a Cary 50 spectrometer from Varian. The emission spectra and relative phosphorescence quantum yields of metal complexes in aerated water were obtained *via* a FLS900 spectrometer from Edinburgh Instruments Ltd. The phosphorescence lifetime of complexes in aerated water was measured by LifeSpec-II from Edinburgh Instruments, with an excitation source of a 375 nm pulsed diode laser (pulse width < 90 ps). The relative singlet oxygen quantum yield (φ_Δ) of complexes was measured in deuterated methanol on a special custom-built setup described previously, with **[Ru(bpy)$_3$]Cl$_2$** (Tris(bipyridine)ruthenium(II) chloride) as the standard (φ_Δ = 0.73).[44, 46]

3.5.5 Calculated values and TDDFT-Calculated spectra of metal complexes. The structures of complexes **[1]**$^+$, **[2]**$^+$, and **[3]**$^{2+}$ were minimized by DFT at the PBE0/TZP level for all atoms including Pd, as implemented in the ADF2017 suite from SCM, using COSMO to simulate

solvent effects (in water), scalar relativistic effects for Pd, no frozen core, and starting from the X-ray structures of **[1]PF_6** and **[2]PF_6**. The 20 first singlet-to-singlet electronic transitions were also calculated with TDDFT using ADF2017 and at the same level of theory, using the Davidson method. Dimer **{[1]$^+$}$_2$** was minimized at the same level of theory as monomer **[1]$^+$**.

3.5.6 Aggregation of metal complexes in different aqueous solutions according to DLS. DLS was chosen to determine the numbers and size of particles in complex solutions (5 and 50 μM) in H_2O, PBS, Opti-MEM medium with and without FCS (fetal calf serum) proteins, via the ZEN1600 Zetasizer Nano instrument (Malvern Instruments Limited) operating with a 633 nm laser.

3.5.7 TEM measurement of metal complexes in different solutions. The TEM experiments were carried out with a TEM JEOL 1010:100 kV transmission electron microscope using Formvar/carbon-coated copper grid from Polysciences Inc. For the preparation of samples, each drop (15 μL) of complex solution was deposited on parafilm. The grids were placed on top of the drops for 2 min and then the excess liquid on the grid was removed with filter paper and dried for 2 h for TEM measurement. The TEM measurements were carried out under vacuum conditions.

3.5.8 Cryo-TEM measurements. sample (6 μL, [complex] = 50 μM) was applied to a freshly glow-discharged carbon 200 mesh Cu grid (lacey carbon film, Electron Microscopy Sciences, Aurion, Wageningen, The Netherlands). Grids were blotted for 3 s at 99% humidity in a Vitrobot plunge-freezer (FEI VitrobotTM Mark III, Thermo Fisher Scientific). Cryo-TEM images were collected on a Talos L120C (NeCEN, Leiden University) operating at 120 kV. Images were recorded manually at a nominal magnification of 4300× or 13500× yielding a pixel size at the specimen of 29.9 or 5.9 Å, respectively.

3.5.9 Cell Culture. Cells were thawed and at least passaged twice before starting cytotoxicity experiments. For normoxia experiments cells were cultured in DMEM completed medium (Dulbecco's Modified Eagle Medium with phenol red, supplemented with 8.0% v/v fetal calf serum (FCS), 0.2% v/v penicillin/streptomycin (P/S), and 1% v/v glutamine), under humidified normoxic conditions (37 °C atmosphere, 21% O_2 and 7.0% CO_2) in 75 cm^2 flasks. They were subcultured upon reaching 70-80% confluence, approximately once per week. Cells were passaged never more than 8 weeks. For the cytotoxicity assay, Opti-MEM complete medium without phenol red was used, supplemented with 2.5% v/v fetal calf serum (FCS), 0.2% v/v penicillin/streptomycin (P/S), and 1% v/v glutamine). For hypoxia cytotoxicity experiments, cells were cultured in DMEM complete medium for at least two weeks in humidified hypoxic

conditions (37 °C atmosphere, 1.0% O_2 and 7.0% CO_2) before starting hypoxic cytotoxicity tests.

3.5.10 Photocytotoxicity assay. The working solutions of the three complexes were typically prepared from 1.0 mM stock solutions of the complex in distilled water. The cell irradiation system consists of a Ditabis thermostat (980923001) fitted with two flat-bottomed microplate thermoblocks (800010600) and a 96-LED array fitted to a standard 96-well plate. The 455 nm LED (FNL-U501B22WCSL), fans (40 mm, 24 V DC, 9714839), and power supply (EA-PS 2042-06B) were ordered from Farnell. A full description of the cell irradiation setup is given in Hopkins et al.[66] The photocytotoxicity assay was carried out via the sulforhodamine B (SRB) assay reports previously.[67] Briefly, a certain number of cells (5000 cells for A549, 8000 cells for A431) were seeded in 96-well plates at t = 0 in a volume of 100 µL of Opti-MEM complete medium without phenol red and incubated for 24 h under normoxic (21% O_2) or hypoxic (1% O_2) conditions. The cells were treated with a freshly prepared solution of the complexes in Opti-MEM at different concentrations in triplicate on the same plates at t =24 h. The concentrations of complexes were tuned depending on their cytotoxicity. At t = 48 h, the irradiation plates were irradiated with blue light under normoxic (455 nm, 5 min, 5.66 mW cm^{-2}, 1.7 J cm^{-2}) or hypoxic (455 nm, 8 min, 3.54 mW cm^{-2}, 1.7 J cm^{-2}) conditions, while the dark plates were kept nonirradiated. After light irradiation, all plates were incubated in the dark for another 48 h under normoxic or hypoxic conditions, respectively. Then, the cells in each well were fixed with trichloroacetic acid (TCA, 10% w/v), gently washed with distilled water, and stained with 100 µL of SRB (0.6% w/v in 1% v/v acetic acid/H_2O solution). The SRB dye was then solubilized with Tris base (10 mM, 200 µL) and the absorbance in each well was read at 510 nm using a M1000 Tecan Reader. Three independent biological replicates were completed for each cell line. The obtained data were analyzed with Graphpad Prism 5 using the dose-response two-parameter Hill-slope equation 1 to obtain the half-maximal effective concentrations EC_{50} (defined as the concentration of drug that gives a half-maximum effect).

$$100/(1 + 10^{log_{10}EC_{50} - X) \times Hill\ Slope}) \quad \textbf{Equation 1}$$

3.5.11 Cellular uptake inhibition. A549 cells (5×10^5 cells) were seeded in six-well plates, incubated for 24 h under normoxic conditions, and then treated with NaN_3 (active uptake inhibitor, 15.4 mM) or dynasore (dynamin-dependent endocytosis inhibitor, 80 µM) for 1 h; after that, the cells were incubated with one of the three palladium complexes (5 µM) for 3 h. To remove the surface-bound drug, the cells were first washed three times using ice-cold PBS. Then the cells were counted via a cell-counting board three times, collected by centrifugation,

and 7 mL of cell lysis buffer (RIPA Lysis and Extraction Buffer, Thermo Scientific™) was added. Ultrasonication was then realized for 3 h at 37 °C to afford clear samples. If precipitation was still observed, HNO_3 (65 % 1 mL) was added to the samples, and the sample was heated for 6 h at 100 °C with a parafilm on the top to prevent solution evaporation. Once back at room temperature, each sample was then diluted with Milli-Q water to reach a volume of 10 mL; this solution was finally injected into a PerkinElmer NexION 2000 ICP-MS to measure the Pd concentration.

3.5.12 Cellular uptake and localization. A549 cells (5×10^5 cells) were seeded in T-75 flasks, incubated for 24 h in Optimum medium at 37 °C under 5% CO_2, and then treated with complexes **[1]OAc−[3](OAc)$_2$**(1 μM, 15 mL), and the control groups were treated with equal volumes of medium. After 24 h of incubation under normoxic conditions, the cells were washed with ice-cold PBS (20 mL) three times and then collected in a 15 mL centrifuge tube and diluted to 10 mL with ice-cold PBS. Then the cells were counted via a cell-counting board three times. Then the Pd contents of the cells were determined by ICP-MS using the same protocol as described above. For cellular fractionation, a FractionPREP Cell Fractionation Kit was used according to the supplier's instructions to prepare the cytosol, membranes, nucleus, and cytoskeleton fractions using the other half of the cell lysis solution. The samples in each fraction were used directly to detect the Pd content by ICP-MS

3.5.13 Measurement of intracellular ROS. The generation of ROS (reactive oxygen species) in A549 cells was measured using the ROS fluorescence indicator, 2,7-dichlorodihydrofluorescein diacetate (DCFH-DA).[19] After acetate cleavage by cellular esterases DCFH-DA can be oxidized by ROS to dichlorofluorescein (DCF), which exhibits strong green fluorescence that can be detected by a fluorescent microscopy or flow cytometry. A549 cells (1×10^5) were seeded into 24-well plates and incubated for 6 h in the dark. The cells were then treated with 5 μM complexes and labeled as dark or blue light groups. After 24 h incubation under normoxia, the medium was refreshed, and the cells were treated with DCFH-DA (20 μM) for 30 min at 37 °C. After that, the blue light group was irradiated with 455 nm blue light for 5 min (5.66 mW cm^{-2}, 1.7 J cm^{-2}). Then the cells were washed with PBS twice, harvested, and centrifuged (3 min × 2000 rpm) to remove supernatant. The cells were resuspended in 200 μL PBS per well in 96-well plate. Untreated cells were maintained as negative controls, whereas a 400 μM H_2O_2 solution in Opti-MEM complete was administered to another set of three wells for 1 h as a positive control for ROS. The levels of intracellular ROS were examined using the Guava easyCyte HT flow cytometer. Gates were applied over

forward scattering, side scattering, and forward scattering area measurements when possible to remove cellular debris and select only for singlet whole cells for further statistical analysis. The GRN-B parameter (488 nm excitation, 525/30 nm emission) was used for fluorescence measurements given its close proximity to the known excitation/emission wavelengths of DCF (498/522 nm, respectively). All flow cytometry data were processed using FlowJ10.

3.5.14 Apoptosis determination. The apoptosis of A549 cells induced by metal complexes was determined with an Annexin V-FITC/propidium iodide double-staining assay. The assay was performed according to the manufacturer's (Bio-Connect BV) protocol. A549 cells were seeded in 6-well plates with 2 mL of Opti-MEM complete medium (2×10^5 cells/well), incubated for 6 h, then treated with the three complexes (15 μM) and cisplatin (15 μM) for 24 h in the dark and under normoxia. Then one plate treated with complexes was irradiated for 5 min with 455 nm blue light (5.66 mW cm^{-2}, 1.7 J cm^{-2}), named as the blue light group. The cells were all further incubated in the dark for 24 h under normoxia, after which cells were harvested and then resuspended in 200 μL 1× annexin binding buffer (purchased from Sanbio B.V.). The resulting cell suspension (200 μL) was stained with 5 μL of Annexin-V-FITC and 5 μL of propidium iodide (purchased from Sanbio B.V) for 15 min at room temperature in the dark, and then detected by flow cytometry immediately. GRN-B Parameter (488 nm excitation, 525±30 nm emission) and RED-B Parameter (488 nm excitation, 661±15 nm emission) were used for fluorescence measurements given their proximity to the known excitation/emission wavelengths of Annexin V-FITC (494/518 nm) and propidium iodide (535/617 nm). All flow cytometry data were processed using FlowJo10.

3.5.15 3D tumor spheroids viability assay. The cytotoxicity of complex **[1]**$^+$ in 3D tumor spheroids was determined with a CellTiter-Glo 3D cell viability assay.[57] A549 cells (500 cells/200 μL per well) were added to a 96-well round-bottomed Corning spheroid plate microplate and centrifuged for 6 min at 800 g to produce tiny tumor spheroid cores that were incubated under normoxia for 120 h to generate 3D tumor spheroids (658±52 μm diameter) At t = 120 h, 100 μL of medium was carefully pipetted out from each well while avoiding the pipetting of spheroids; then the spheroids were immediately treated with 100 μL of an Opti-MEM complete medium solution of complex **[1]**$^+$ with a range of concentrations to reach final concentrations in the wells of 0, 2, 10, 20, 40, 100, and 200 μM. Each concentration was repeated in technical triplicate on the same plate. The spheroids were incubated further under normoxia. At t = 144 h, one plate was irradiated with blue light under air (455 nm, 10 min, 3.48 mW cm^{-2}, 2.1 J cm^{-2}), and the other was left in the dark in a normoxic incubator. The spheroids

were further incubated under normoxia in the dark. At t = 192 h, a CellTiter Glo 3D solution (100 μL/well) was added to each well to stain the 3D tumor spheroids. After 30 min of shaking on an IKA Vibrax shaker at 500 rpm at room temperature, the luminescence in each well was measured with a Tecan microplate reader. Half-maximal effective concentrations (EC_{50}) for 3D tumor spheroid growth inhibition were calculated by fitting the CellTiter Glo3D dose-response curves using the same non-linear regression function as in 2D (Equation 1) as implemented in Graphpad Prism 5.

3.5.16 *In vivo* experiments. Tumor-bearing female BALB/c mice were originally purchased from Vital River Laboratory Animal Center (Beijing, China). The mice were kept under specific pathogen-free conditions with free access to standard food and water. This study was conducted in accordance with the Guide for the Care and Use of Laboratory Animals published by the U.S. National Institutes of Health (8th edition, 2011). All protocols for animal studies conformed to the Guide for the Care and Use of Laboratory Animals. All animal experiments were performed following guidelines approved by the ethics committee of Peking University. The tumor model was established by injecting 1×10^7 of 4T1 breast cells suspended in 100 μL of PBS into the right flank region of each mouse to obtain a mouse 4T1 breast tumor implant. The tumor volume (V) can be calculated with equation $V = L/2 \times W^2$ after measuring the tumor length (L) and width (W) using a vernier caliper.[68] The mice were randomly divided into six groups (control, 450 nm light, **[1]**$^+$ dark, **[2]**$^+$ dark, **[1]**$^+$ + 450 nm light, and **[2]**$^+$ + 450 nm light groups) when the tumor volume reached about 40 mm^3. The mice were treated through paracancerous injection with saline (control and 450 nm light groups), **[1]**$^+$ (40 μM, 100 μL, 0.01 mg/kg) and **[2]**$^+$ (40 μM, 100 μL, 0.01 mg/kg). One hour after injection, 450 nm irradiation (50 mW cm^{-2}, 20 min, 60 J cm^{-2}) was then carried out in 450 nm irradiation, **[1]**$^+$ **+ 450 nm**, and **[2]**$^+$ **+ 450 nm** groups. The tumor volume and body weight of each mouse were measured and recorded, and the average tumor volume and body weight were calculated (N=3) over a period of 10 days.

3.6 References

1. P. Štarha, J. Vančo and Z. Trávníček, *Coord. Chem. Rev.*, 2019, **380**, 103-135.
2. S. Dilruba and G. V. Kalayda, *Cancer Chemother. Pharmacol*, 2016, **77**, 1103-1124.
3. X. Wang and Z. Guo, *Chem. Soc. Rev.*, 2013, **42**, 202-224.
4. R. J. Browning, P. J. T. Reardon, M. Parhizkar, R. B. Pedley, M. Edirisinghe, J. C. Knowles and E. Stride, *ACS Nano*, 2017, **11**, 8560-8578.
5. S. Dasari and P. B. Tchounwou, *Eur. J. Pharmacol.*, 2014, **740**, 364-378.
6. B. Li, Z. Meng, Q. Li, X. Huang, Z. Kang, H. Dong, J. Chen, J. Sun, Y. Dong, J. Li, X. Jia, J. L. Sessler, Q. Meng and C. Li, *Chem. Sci.*, 2017, **8**, 4458-4464.
7. K. S. Lovejoy and S. J. Lippard, *Dalton Trans.*, 2009, 10651-10659.

8. E. Petruzzella, R. Sirota, I. Solazzo, V. Gandin and D. Gibson, *Chem. Sci.*, 2018, **9**, 4299-4307.
9. R. Oun, Y. E. Moussa and N. J. Wheate, *Dalton Trans.*, 2018, **47**, 6645-6653.
10. L. Galluzzi, L. Senovilla, I. Vitale, J. Michels, I. Martins, O. Kepp, M. Castedo and G. Kroemer, *Oncogene*, 2012, **31**, 1869-1883.
11. J. N. Liu, W. Bu and J. Shi, *Chem. Rev.*, 2017, **117**, 6160-6224.
12. S. Mallidi, S. Anbil, A. L. Bulin, G. Obaid, M. Ichikawa and T. Hasan, *Theranostics*, 2016, **6**, 2458-2487.
13. S. Monro, K. L. Colon, H. Yin, J. Roque, 3rd, P. Konda, S. Gujar, R. P. Thummel, L. Lilge, C. G. Cameron and S. A. McFarland, *Chem. Rev.*, 2019, **119**, 797-828.
14. A. P. Castano, T. N. Demidova and M. R. Hamblin, *Photodiagn. Photodyn. Ther.*, 2004, **1**, 279-293.
15. P. Agostinis, K. Berg, K. A. Cengel, T. H. Foster, A. W. Girotti, S. O. Gollnick, S. M. Hahn, M. R. Hamblin, A. Juzeniene, D. Kessel, M. Korbelik, J. Moan, P. Mroz, D. Nowis, J. Piette, B. C. Wilson and J. Golab, *CA: Cancer J. Clin.*, 2011, **61**, 250-281.
16. T. He, C. Ren, Y. Luo, Q. Wang, J. Li, X. Lin, C. Ye, W. Hu and J. Zhang, *Chem. Sci.*, 2019, **10**, 4163-4168.
17. T. L. Lam, K. C. Tong, C. Yang, W. L. Kwong, X. Guan, M. D. Li, V. Kar-Yan Lo, S. Lai-Fung Chan, D. Lee Phillips, C. N. Lok and C. M. Che, *Chem. Sci.*, 2019, **10**, 293-309.
18. Z. Dong, L. Feng, Y. Hao, M. Chen, M. Gao, Y. Chao, H. Zhao, W. Zhu, J. Liu, C. Liang, Q. Zhang and Z. Liu, *J. Am. Chem. Soc.*, 2018, **140**, 2165-2178.
19. Z. Lv, H. Wei, Q. Li, X. Su, S. Liu, K. Y. Zhang, W. Lv, Q. Zhao, X. Li and W. Huang, *Chem. Sci.*, 2018, **9**, 502-512.
20. H. Huang, P. Zhang, H. Chen, L. Ji and H. Chao, *Chem. Eur. J.*, 2015, **21**, 715-725.
21. F. Heinemann, J. Karges and G. Gasser, *Acc. Chem. Res.*, 2017, **50**, 2727-2736.
22. L. Salassa, *Eur. J. Inorg. Chem.*, 2011, **2011**, 4931-4947.
23. K. Arora, M. Herroon, M. H. Al-Afyouni, N. P. Toupin, T. N. Rohrabaugh, L. M. Loftus, I. Podgorski, C. Turro and J. J. Kodanko, *J. Am. Chem. Soc.*, 2018, **140**, 14367-14380.
24. T. J. Whittemore, A. Millet, H. J. Sayre, C. Xue, B. S. Dolinar, E. G. White, K. R. Dunbar and C. Turro, *J. Am. Chem. Soc.*, 2018, **140**, 5161-5170.
25. M. Clement, G. Daniel and M. Trelles, *J. Cosmet. Laser. Ther.*, 2005, **7**, 177-189.
26. G. Ghosh, K. L. Colon, A. Fuller, T. Sainuddin, E. Bradner, J. McCain, S. M. A. Monro, H. Yin, M. W. Hetu, C. G. Cameron and S. A. McFarland, *Inorg. Chem.*, 2018, **57**, 7694-7712.
27. A. Notaro, G. Gasser and A. Castonguay, *ChemMedChem*, 2020, **15**, 345-348.
28. J. L. Tsai, T. Zou, J. Liu, T. Chen, A. O. Chan, C. Yang, C. N. Lok and C. M. Che, *Chem. Sci.*, 2015, **6**, 3823-3830.
29. K. Suntharalingam, J. J. Wilson, W. Lin and S. J. Lippard, *Metallomics*, 2014, **6**, 437-443.
30. A. Wragg, M. R. Gill, L. McKenzie, C. Glover, R. Mowll, J. A. Weinstein, X. Su, C. Smythe and J. A. Thomas, *Chem. Eur. J.*, 2015, **21**, 11865-11871.
31. C. N. Lok, T. Zou, J. J. Zhang, I. W. Lin and C. M. Che, *Adv. Mater.*, 2014, **26**, 5550-5557.
32. K. Qiu, Y. Chen, T. W. Rees, L. Ji and H. Chao, *Coord. Chem. Rev.*, 2019, **378**, 66-86.
33. P. Wu, E. L. Wong, D. L. Ma, G. S. Tong, K. M. Ng and C. M. Che, *Chem. Eur. J.*, 2009, **15**, 3652-3656.
34. L. Shang, K. Nienhaus and G. U. Nienhaus, *J. Nanobiotechnol.*, 2014, **12**, 1-11.
35. A.-R. Azzouzi, S. Vincendeau, E. Barret, A. Cicco, F. Kleinclauss, H. G. van der Poel, C. G. Stief, J. Rassweiler, G. Salomon, E. Solsona, A. Alcaraz, T. T. Tammela, D. J. Rosario, F. Gomez-Veiga, G. Ahlgren, F. Benzaghou, B. Gaillac, B. Amzal, F. M. J. Debruyne, G. Fromont, C. Gratzke and M. Emberton, *Lancet Oncol.*, 2017, **18**, 181-191.
36. X. Q. Zhou, A. Busemann, M. S. Meijer, M. A. Siegler and S. Bonnet, *Chem. Comm.*, 2019, **55**, 4695-4698.
37. K. T. Chan, G. S. M. Tong, Q. Wan, G. Cheng, C. Yang and C. M. Che, *Chem. Asian J.*, 2017, **12**, 2104-2120.
38. J. M. Hope, J. J. Wilson and S. J. Lippard, *Dalton Trans.*, 2013, **42**, 3176-3180.
39. J.-L. Li, L. Jiang, B.-W. Wang, J.-L. Tian, W. Gu, X. Liu and S.-P. Yan, *New J. Chem.*, 2015, **39**, 529-538.
40. C. Zou, J. Lin, S. Suo, M. Xie, X. Chang and W. Lu, *Chem. Comm.*, 2018, **54**, 5319-5322.

41. A. Aliprandi, M. Mauro and L. De Cola, *Nat. Chem.*, 2016, **8**, 10-15.
42. Q. Wan, J. Xia, W. Lu, J. Yang and C. M. Che, *J. Am. Chem. Soc.*, 2019, **141**, 11572-11582.
43. X. Yin, S. A. Warren, Y. T. Pan, K. C. Tsao, D. L. Gray, J. Bertke and H. Yang, *Angew Chem. Int. Ed.*, 2014, **53**, 14087-14091.
44. M. C. DeRosa and R. J. Crutchley, *Coord. Chem. Rev.*, 2002, **233-234**, 351-371.
45. A. M. Brouwer, *Pure Appl. Chem.*, 2011, **83**, 2213-2228.
46. J. A. Cuello-Garibo, M. S. Meijer and S. Bonnet, *Chem. Comm.*, 2017, **53**, 6768-6771.
47. P. Swietach, R. D. Vaughan-Jones, A. L. Harris and A. Hulikova, *Philos. Trans. R. Soc. B*, 2014, **369**, 20130099.
48. J.-Y. Lee, M.-C. Tsai, P.-C. Chen, T.-T. Chen, K.-L. Chan, C.-Y. Lee and R.-K. Lee, *J. Phys. Chem. C*, 2015, **119**, 25754-25760.
49. S. Zhang, J. Li, G. Lykotrafitis, G. Bao and S. Suresh, *Adv. Mater.*, 2009, **21**, 419-424.
50. L. Kou, J. Sun, Y. Zhai and Z. He, *Asian J. Pharm. Sci.*, 2013, **8**, 1-10.
51. M. S. Meijer, V. S. Talens, M. F. Hilbers, R. E. Kieltyka, A. M. Brouwer, M. M. Natile and S. Bonnet, *Langmuir*, 2019, **35**, 12079-12090.
52. J. Karges, P. Goldner and G. Gasser, *Inorganics*, 2019, **7**.
53. J. Zhao and M. H. Stenzel, *Polym. Chem.*, 2018, **9**, 259-272.
54. J. Yang, J. Tu, G. E. M. Lamers, R. C. L. Olsthoorn and A. Kros, *Adv. Healthc. Mater.*, 2017, **6**.
55. P. Mroz, A. Yaroslavsky, G. B. Kharkwal and M. R. Hamblin, *Cancers*, 2011, **3**, 2516-2539.
56. G. Lazzari, P. Couvreur and S. Mura, *Polym. Chem.*, 2017, **8**, 4947-4969.
57. M. Zanoni, F. Piccinini, C. Arienti, A. Zamagni, S. Santi, R. Polico, A. Bevilacqua and A. Tesei, *Sci. Rep.*, 2016, **6**, 19103.
58. E. V. Maytin, U. Kaw, M. Ilyas, J. A. Mack and B. Hu, *Photodiagn. Photodyn. Ther.*, 2018, **22**, 7-13.
59. P. Gholam, I. Bosselmann, A. Enk and C. Fink, *J. Dtsch. Dermatol. Ges.*, 2018, **16**, 711-717.
60. P. Oltulu, B. Ince, N. Kokbudak, S. Findik and F. Kilinc, *Turk. J. Plast. Surg.*, 2018, **26**.
61. C. Ash, M. Dubec, K. Donne and T. Bashford, *Lasers Med. Sci.*, 2017, **32**, 1909-1918.
62. H. Zheng, *Technol. Cancer Res. T.*, 2005, **4**, 283-293.
63. P. Kaspler, S. Lazic, S. Forward, Y. Arenas, A. Mandel and L. Lilge, *Photochem. Photobiol. Sci.*, 2016, **15**, 481-495.
64. Q. Wan, W. P. To, C. Yang and C. M. Che, *Angew Chem. Int. Ed.*, 2018, **57**, 3089-3093.
65. M. Wehner and F. Würthner, *Nat. Rev. Chem.*, 2019, **4**, 38-53.
66. S. L. Hopkins, B. Siewert, S. H. Askes, P. Veldhuizen, R. Zwier, M. Heger and S. Bonnet, *Photochem. Photobiol. Sci.*, 2016, **15**, 644-653.
67. V. Vichai and K. Kirtikara, *Nat. Protoc.*, 2006, **1**, 1112-1116.
68. W. Sun, J. Fan, S. Wang, Y. Kang, J. Du and X. Peng, *ACS Appl. Mater. Interfaces*, 2018, **10**, 7832-7840.